

7-2011

Novel catalyst for the removal of aromatic sulfur species from refinery streams.

Franz Georg Petzold 1979-
University of Louisville

Follow this and additional works at: <http://ir.library.louisville.edu/etd>

Recommended Citation

Petzold, Franz Georg 1979-, "Novel catalyst for the removal of aromatic sulfur species from refinery streams." (2011). *Electronic Theses and Dissertations*. Paper 1122.
<https://doi.org/10.18297/etd/1122>

This Master's Thesis is brought to you for free and open access by ThinkIR: The University of Louisville's Institutional Repository. It has been accepted for inclusion in Electronic Theses and Dissertations by an authorized administrator of ThinkIR: The University of Louisville's Institutional Repository. This title appears here courtesy of the author, who has retained all other copyrights. For more information, please contact thinkir@louisville.edu.

NOVEL CATALYST FOR THE REMOVAL
OF AROMATIC SULFUR SPECIES FROM REFINERY STREAMS

By

Franz Georg Petzold
B.S., University of Louisville, 2010

A Thesis
Submitted to the Faculty of the
University of Louisville
J. B. Speed School of Engineering
as Partial Fulfillment of the Requirements
for the Professional Degree

MASTER OF ENGINEERING

Department of Chemical Engineering

July 2011

NOVEL CATALYST FOR THE REMOVAL
OF AROMATIC SULFUR SPECIES FROM REFINERY STREAMS

Submitted by: _____
Franz Georg Petzold

A Thesis Approved on

by the Following Reading and Examination Committee:

Dr. Mahendra Sunkara

Dr. Moises Carreon

Dr. Gamini Sunanasekera

ACKNOWLEDGEMENTS

I am very thankful to my supervisor, Dr. Mahendra Sunkara, whose encouragement, guidance, and support throughout the entire process has enabled me to advance in my academic development.

I owe my gratitude to Dr. Helge Toufar, without whom this thesis would not have been possible. He sparked the interest in utilizing nanowires for catalysis and has been supportive in a number of ways vital to the success of the project.

I would like to thank Dr. Moises Carreon and Dr. Paul Ratnasamy for expert advice relating to fundamental concerns regarding catalysis in general, which helped me tremendously in developing an understanding of the subject.

I would like to express appreciation of the efforts of Dr. Jacek Jasinski, Dr. Chinmay Deshmane, and Chandrashekhler Pendyala, who helped me explore and utilize valuable possibilities relating to materials characterization.

Furthermore, I am indebted to many of my colleagues who supported me with indispensable practical tasks. Among them, I would like to explicitly mention Peter Houge, Todd Cole, Ezra Clark, Jason Absher, and Minqi Zhu.

Lastly, I offer my deepest gratefulness to my wife, Lou Ann, without whose support and encouragement I would not have reached this stage in my life.

ABSTRACT

A novel catalyst with hydro-desulfurization and hydrogenation capabilities was tested with the aim of producing ultra-low sulfur and aromatics diesel oil. The catalytically active phase is nickel in a reduced valence state on a carrier made of zinc oxide nanowires and alumina. Based on the reactive adsorption principle, it was speculated that enhanced metal-support interactions and short diffusion paths between nickel and zinc oxide could lead to improved activity and sulfur uptake capacity. Zinc oxide nanowires, proposed here as a novel catalyst support, were produced in appreciable quantities in a microwave-induced plasma jet reactor. After purification and decoration with an active nickel phase, the nanowires underwent extensive characterization, which revealed promising properties. On-stream hydrogenation activity and sulfur uptake was tested on a model diesel oil spiked with difficult-to-remove organic sulfur species. It was observed that the proposed catalyst system, as it was assembled in this project, is inferior to existing hydro-desulfurization products. Nevertheless, this undertaking was a first crude attempt and the concept of reactive adsorption was sufficiently demonstrated, which can hopefully be improved upon with succeeding trials.

TABLE OF CONTENTS

	<u>Page</u>
APPROVAL PAGE.....	ii
ACKNOWLEDGEMENTS.....	iii
ABSTRACT.....	iv
TABLE OF CONTENTS.....	v
LIST OF TABLES.....	vii
LIST OF FIGURES.....	viii
I. INTRODUCTION.....	1
<u>Definition Of The Problem</u>	2
<u>Motivation To Utilize Nanowires</u>	7
II. ZINC OXIDE NANOWIRE PRODUCTION AND PURIFICATION.....	9
<u>Equipment And Procedures</u>	9
<u>Zinc Oxide Nanowire Growth Mechanism</u>	11
<u>ZnO NW Purification</u>	13
<u>Electro-Kinetic Potential</u>	14
<u>Separation Procedure</u>	19
<u>Examination of Suspension Behavior</u>	19
III. CATALYST PREPARATION AND CHARACTERIZATION.....	22
<u>Choice Of Nickel Salt</u>	23
<u>TGA/DSC Decomposition Temperature And Nickel Wetting</u>	23
<u>Phase Identification Of Calcined Product Via XRD Signatures</u>	26
<u>Morphology Assessment Via SEM</u>	27

	<u>TEM And EDS Mapping Of Individual ZnO NW</u>	28
	<u>TEM In-Situ Decomposition Of NiAc On ZnO NWs</u>	29
	<u>Analysis Of NiO NP – ZnO NW Interaction Via TPR And Hot Stage</u>	
	<u>XRD</u>	33
	<u>Sulfur Uptake Confirmation Via XRD</u>	36
	<u>Crush Strength Test Of Catalyst Extrusions</u>	37
	<u>Final Catalyst Preparation</u>	38
IV.	ACTIVITY AND HYDRODESULFURIZATION TEST.....	40
	<u>Feed Composition</u>	40
	<u>Reactor Loading</u>	41
	<u>Activity Test</u>	42
	<u>Aromatics Breakthrough</u>	42
	<u>Sulfur Breakthrough</u>	44
V.	CONCLUSIONS AND RECOMMENDATIONS.....	45
	REFERENCES.....	48
	APPENDIX.....	53
	<u>Supplementary Tables and Figures</u>	53
	<u>Raw Data</u>	57
	<u>Photographs</u>	59
	VITA.....	61

LIST OF TABLES

	<u>Page</u>
TABLE I ORGANO-SULFUR COMPOUNDS WITH HDS REACTION CONSTANTS.....	53
TABLE II OVERVIEW OF CATALYST PARTICLE DIMENSIONS, SELECTED REPORTS.....	54
TABLE III NANOWIRE SURFACE AREA AND NICKEL LOADING.....	55
TABLE IV REACTOR LOADING SPECIFICATIONS.....	41
TABLE V PRODUCT SAMPLE DILUTION AND UV/VIS RECORD.....	57

LIST OF FIGURES

	<u>Page</u>
FIGURE 1 – Illustration of Microwave Plasma Jet Reactor.....	10
FIGURE 2 – Illustration of ZnO NW Growth out of Molten Zinc Droplet.....	11
FIGURE 3 – SEM micrographs of ZnO NWs Protruding out of Droplets.....	12
FIGURE 4 – SEM Images of Fresh ZnO NW.....	13
FIGURE 5 – Zeta Potential of ZnO NWs and NPs at Different pH Values.....	15
FIGURE 6 –Representative SEM Images of Commercial ZnO NPs (a, b, c) and HRTEM Image of a ZnO NW (d) with Incident Electron Beam along {2-1-10} Direction.....	18
FIGURE 7 – ZnO Junk-NPs from Bottom Cake (a, b) and ZnO NWs from Suspension (c, d).....	20
FIGURE 8 – TGA/DSC Curves for NiAc Decomposition on ZnO NWs.....	25
FIGURE 9 – XRD Patterns of Hexagonal Wurtzite ZnO (blue) and Face-Centered Cubic Bunsenite (red) Phases with Plane Indices.....	26
FIGURE 10 –SEM Images of Calcined ZnO NWs with 30% Nickel Over-Loading on a Gold-Coated Quartz Substrate.....	27
FIGURE 11 – TEM of NiO NPs Affixed to and Detached from ZnO NWs (a), HRTEM Close-Up and Selected Area Electron Diffraction (b).....	28
FIGURE 12 – HRTEM Image and EDS Maps of a Single NW for Individual Elements.....	29
FIGURE 13 – Representative SEM Images of ZnO NWs Coated with NiAc.....	31

FIGURE 14 – TEM Images of In-Situ Calcined NiAc on ZnO NWs (a, b, c), Images (d) and (e) are Close-Ups of (a) and (b), (f) is a Close-Up of (c), (g) is a Close-Up of (f).....	32
FIGURE 15 – TPR Curves for NiO on ZnO NPs and ZnO NWs.....	34
FIGURE 16 – Mean Crystallite Sizes of Nickel on ZnO Carriers from Hot Stage XRD Data.....	35
FIGURE 17 – XRD Patterns of Hexagonal ZnO (red) and Cubic ZnS (blue).....	36
FIGURE 18 – Representative SEM Images of ZnO NWs after Exposure to H ₂ S.....	37
FIGURE 19 – Reactor Schematic.....	41
FIGURE 20 – Aromatics Breakthrough of Two Commercial Catalysts and Ni/ZnO NW/Al ₂ O ₃	43
FIGURE 21 – Sulfur Uptake Curves of Two Commercial Catalysts and Ni/ZnO NW/Al ₂ O ₃	44
FIGURE 22 – NiO/ZnO NW Reduction Signal under 5% Hydrogen Hot Stage XRD.....	58
FIGURE 23 – NiO/ZnO NP Reduction Signal under 5% Hydrogen Hot Stage XRD.....	58
FIGURE 24 – Unit Diagram for Hydrogenation Test Reactor.....	56
FIGURE 25 – Photographs of Hydrogenation Test Unit.....	59
FIGURE 26 – Photographs of the Extrusion Production Process.....	60

I. INTRODUCTION

Considering increasingly stringent environmental legislation to reduce sulfur concentrations in transport fuels, it is apparent that the world is on a sulfur-free fuels trajectory. The reduction of gasoline and diesel sulfur is an important means for improving air quality because of the negative impact sulfur has on the performance of automotive engine exhaust inhibitors as it irreversibly poisons noble metal catalysts in the converter. Aside from the legislative pressure, the demand for ultra-low sulfur fuels has also naturally been driven by the growing application of fuel cells. Due to their high energy density, ease of storage, and well-established distribution-infrastructure, transportation fuels such as gasoline, jet fuel, and diesel are perfect candidates for high efficiency fuel cells. Nevertheless, to protect the reforming catalyst and the electrodes of the fuel cell system from deactivation, the sulfur concentration of the fuel needs to be ultra-low (<0.1 ppm). In light of the legislative developments to prevent emissions of sulfur oxides as well as the general emergence of ultra-low sulfur applications, ultra-deep desulfurization of gasoline and diesel oil has become an increased focus of research with many diverse approaches. The subject matter of this paper is to present a

novel reactive adsorption route utilizing nickel decorated zinc oxide nanowires for ultra-deep desulfurization of light and middle refinery distillates.

Definition Of The Problem

Refinery streams like naphtha, kerosene, diesel oil and heavier oils contain a wide range of organic sulfur compounds, among others mercaptanes, thiophenes, organic sulfides and disulfides. These organic sulfur compounds are products of the degradation of sulfur-containing biological components, present during the natural formation of the fossil fuel, petroleum crude oil. Part of the environmental and legislative motivation behind lowering sulfur concentrations in transportation fuels is that combustion of such sulfur-bearing species results in sulfur oxides which when released into the atmosphere cause acid rain. As of 2006, the total sulfur limit for highway diesel is in the range of 15 to 30 ppm by weight. Notwithstanding legislative efforts, low sulfur concentrations are desirable from an operational standpoint for refineries. The catalytic conversion of hydrocarbon streams into hydrogen-rich gas (e.g. steam reforming, auto-thermal-reforming, and partial oxidation) is extremely sulfur sensitive. Even in minute concentrations, sulfur poisons (deactivates) the noble metal catalysts which therefore require frequent regeneration or replacement. The conventional hydrodesulfurization (HDS) process utilizes alumina- and silica-supported cobalt or nickel molybdenum catalyst. However, sulfur levels after conventional HDS treatment are still too high for these downstream sulfur-sensitive applications. Most of

the “benign” non-cyclic sulfur compounds present in the aforementioned refinery streams can be dealt with in conventional HDS. The challenging compounds are heterocyclic compounds like thiophenes; benzo-thiophenes; substituted, condensed ring, and sterically hindered dibenzo-thiophenes; which are difficult to remove due to their aromaticity and consequent low reactivity. A list of “difficult” sulfur compounds and their HDS reaction constants can be found in TABLE I in the appendix.

Typical catalysts for hydrogenation and hydrodesulfurization are transition metals of the Group-9 and Group-10 elements, displaying vacant d-orbitals such as cobalt ($3d^7$), nickel ($3d^8$), rhodium ($4d^8$), palladium ($4d^{10}$), and platinum ($5d^9$). Nickel and cobalt on various promoters and supports are almost exclusively encountered in industrial refinery columns rather than noble platinum group metals for obvious economic reasons. Carbon-heteroatom cleavage under hydrogen pressure is achieved via a classical hydrogenolysis reaction scheme. In a hydrogen atmosphere, the metal active phase, i.e. nickel, is able to cleave the sulfur off the “difficult” cyclic compounds; thereby converting the sulfur into hydrogen sulfide (H_2S). Nonetheless, the active nickel phase is slowly poisoned by the resulting H_2S forming nickel sulfide according to the following reaction:



As nickel converts to nickel sulfide, catalytic activity decreases and eventually extinguishes completely. In industry, the catalyst will either have to be regenerated or

replaced once a certain threshold breakthrough of sulfur is detected in the product stream.

There are several actively researched alternative methods which aim at removing sulfur levels to below ten parts per million. Song (2003), Ito (2006) and Stanislaus (2010) summarized the most prominent research areas, which include oxidative routes for diesel, chemical conversion methods, non-destructive adsorption, extraction, biodesulfurization, and reactive adsorption. The concept behind reactive adsorption is that once a conventional metal active phase of a catalyst converts all “difficult” organic sulfur species under hydrogen to H_2S , an adsorptive phase, usually the base oxide support material, accepts and permanently stores the sulfur portion of the H_2S . The permanent storage capacity is important, as H_2S , when present downstream of the catalyst adsorbent, tends to recombine with olefins in the product steam to mercaptanes. In order to find a suitable adsorbent carrier, several materials have been inspected based on simple thermodynamic favorability considerations (Gibbs free energies). Copper, zinc, and their respective oxides appear to be the only candidates to hold practical feasibility. Copper oxide shows great acceptor potential; however, it cannot exist in oxide form in a hydrogen atmosphere at operating temperatures as it readily reduces back to metallic copper. Zinc oxide, which is the focus of this paper, exhibits great stability in hydrogen and is thermodynamically favored to accept sulfur. Provided that H_2S has a short diffusion path, the following reaction describes the driving force behind the regeneration mechanism proposed in this paper:



Of the several groups that have published work on the Ni/ZnO system, Tawara (2000, 2001), Bezverkhy (2007), Lee (2007), Matthias (2007), Ryzhikov (2008), Da Costa-Serra (2010), Fan (2010), Zhang (2010), and Huang (2010, 2011) are relevant to the proposed approach. The key concept in reactive adsorption with nickel on a zinc oxide carrier is that it combines catalytic HDS and adsorption desulfurization where the sulfur poisoned nickel active sites are regenerated by the zinc oxide. The challenge is to create a catalyst with high desulfurization activity, high selectivity towards sulfur-containing compounds, and high sulfur capacity.

There are several factors that drastically influence the performance of the reactive adsorbent. A high surface area is required to utilize as much of the active metal phase as possible. Further, a small crystallite size is desirable as particle size and catalytic activity are generally inversely related. The general goal is to achieve a high dispersion of the metal active phase and to keep it dispersed throughout the life time of the catalyst. Lastly, a weak inclination of the catalyst towards sintering during the calcination step, reduction step, and operating conditions at high temperatures is very advantageous to maintain both the surface area and small crystallite size. Sintering is the loss of active surface area due to crystal growth of either the bulk material or the active phase which is strongly temperature dependent but also affected by the surrounding gas atmosphere. Other factors that influence the mobility of the solid phase are texture, size and morphology, time on stream, metal loading, and carrier

composition. In the case of supported transition metal catalysts, agglomeration and coalescence of small metal crystallites into larger ones cause severe reduction of surface area and activity. Two major modes of sintering have generally been proposed; the atomic migration model and the crystallite migration model. The latter occurs via migration of the crystallites along the surface, followed by collision and coalescence of two crystallites. However, given the relevant temperature range for the proposed reactive adsorbent, the atomic migration model is probably a more appropriate description for the investigated sintering phenomena. As such, migration of metal atoms occurs via the surface or gas phase by diminishing small crystallites in size and increasing the larger ones. The so-called Hüttig and Tammann temperatures indicate the temperature at which sintering starts. The following semi-empirical relations for Hüttig and Tamman temperatures are commonly used:

$$T_{\text{Hüttig}} = 0.3 T_{\text{melting}} \quad \text{Atomic Migration} \quad (3)$$

$$T_{\text{Tammann}} = 0.5 T_{\text{melting}} \quad \text{Crystallite Migration} \quad (4).$$

The Ni/ZnO system considered here has a Hüttig temperature of $0.3 \times 1728\text{K} = 245^\circ\text{C}$ and a Tammann temperature of $0.5 \times 1728\text{K} = 591^\circ\text{C}$. Both temperatures become relevant for the calcination and reduction procedure in the experimental section.

Motivation To Utilize Nanowires

The class of catalysts/adsorbents currently used or tested for ultra-deep HDS is typically prepared by co-precipitation or (incipient wetness) impregnation of the support from an aqueous solution containing a suitable precursor compound. Both particles ZnO and Ni(O) are initially very small. However, after calcination and during reduction and operation, sintering severely deteriorates the desired particle properties. For an overview of reported particle dimensions, refer to TABLE II in the appendix.

As suggested by Da Costa-Serra (2010), the morphology and particle size of the ZnO support can influence the catalytic behavior of the supported nickel. He showed how the morphology, shape, and size of ZnO support particles can control the impregnation process of the metal active centers, which manages the properties of active metallic particles. It has been found that nanorod particles of ZnO, obtained by calcination of zinc acetate, favor metal-support interactions, decreasing the metallic particle sizes and avoiding metal sintering during the calcination of metal precursors. Small metallic particle sizes lead to high values of active metal exposure surface, thereby increasing the catalytic activity. Da Costa-Serra's group impregnated nickel onto several ZnO supports with varying morphologies and then calcined, reduced, and tested the products for activity. It appears that small spherical ZnO particles tend to readily sinter upon calcination and reduction; which, consequently, produces larger and less catalytically active nickel particles. All samples with initial small spherical morphologies seem to favor the mobility of the metal cat-ions over the support surface. The ZnO

support sample comprised of nanorods (600 x 80 nm), however, appears to be very resistant to sintering as its dimensions remain unaffected after calcination. A consequent temperature programmed reduction (TPR) study confirmed that the metal-support interaction between nickel and the ZnO nanorod support is considerably greater than with ZnO nanoparticle (NP) supports.

Inspired by the high sintering resistance caused by the morphology of the rod-like ZnO support, it was compelling to go a step further and attempt to exploit the properties of ZnO nanowires (NWs). Through the work of Kim (2008), Kumar (2008), and Clark (2011), the prospect of large scale production of transition metal oxide NWs became cautiously feasible. Given the outlook of bulk production of ZnO NWs, they could lend themselves to be employed as superior catalyst supports.

This paper is broken down into three sections, as follows: it first briefly explains the production and purification process of ZnO NWs; it then describes the Ni/ZnO NW catalyst preparation and characterization; and, finally, it evaluates activity and sulfur uptake testing. As this approach is without published precedence, all rationales for steps taken will be stated accordingly.

II. ZINC OXIDE NANOWIRE PRODUCTION AND PURIFICATION

Equipment And Procedures

A microwave plasma jet reactor as described by Kim (2008) was employed to produce sufficiently large quantities of ZnO NWs within the order of magnitude of grams per day. The essential components of the reactor arrangement are schematically depicted in FIGURE 1.

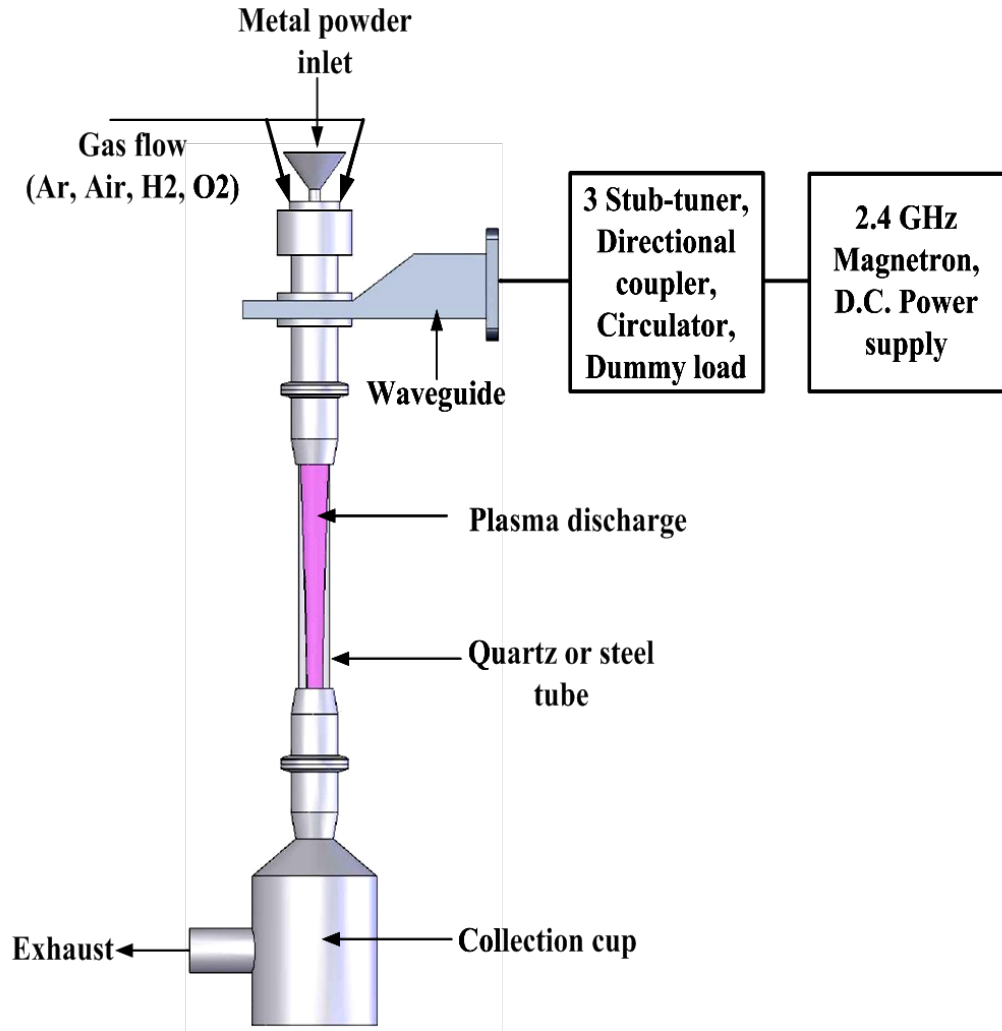


FIGURE 1 – Illustration of Microwave Plasma Jet Reactor

The existing reactor arrangement was improved with a smart-match that automatically reflects all reversely scattered microwaves back toward the waveguide. Furthermore, a water-cooled feed entrance system and a two-stage vibrating metal powder feeder were installed, which secures a steady and well-dispersed stream of zinc NP powder. The conditions for optimal production runs were found by trial and error.

Zinc Oxide Nanowire Growth Mechanism

The Zn NPs with diameters ranging from 10 to 15 nm are converted to ZnO NWs as they fall through a microwave-induced atmospheric plasma plume. The growth mechanism can briefly be described as nucleation and bottom up growth of supersaturated ZnO out of liquid zinc droplets. Upon entering the dense plasma plume, radical recombination causes the Zn NP to melt into droplets almost immediately, as it releases a lot of heat ($\Delta H = -505.3$ kJ/mol). Oxygen radicals diffuse into the Zn droplets where they readily oxidize Zn into ZnO. At the point at which the ZnO supersaturates within the Zn droplet, ZnO nuclei simultaneously spear through the Zn droplet surface. As the radical flux into the Zn droplet continues to produce more ZnO, the surface ZnO nuclei start growing outwards as single crystal nanowires are being fed more ZnO from the bottom. ZnO on Zn has low wettability and, therefore, grows nearly perpendicularly out of the Zn droplet. The ZnO NWs are of hexagonal wurtzite phase with a growth direction exclusively along the c-axis, which exposes the $\{01\bar{1}0\}$ and $\{2\bar{1}10\}$ planes.

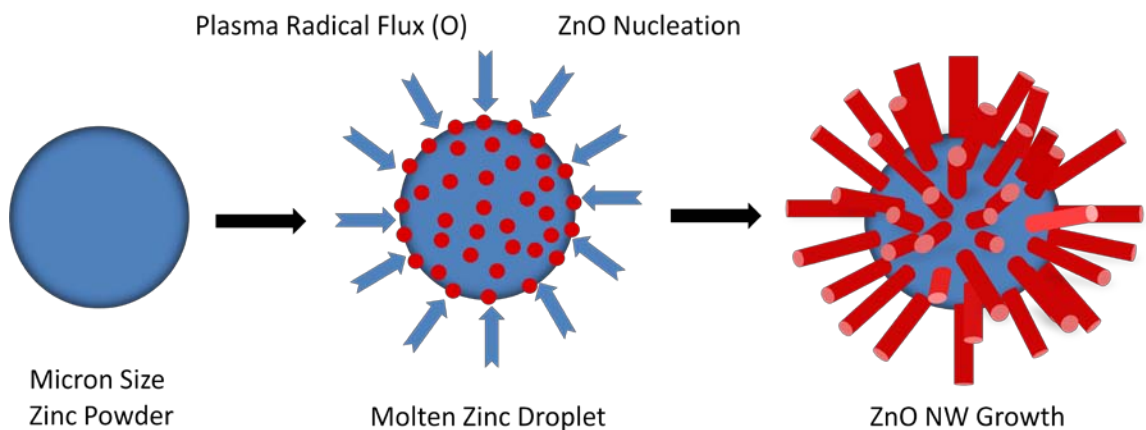


FIGURE 2 – Illustration of ZnO NW Growth out of Molten Zinc Droplet

ZnO NW growth ceases when all Zn within the Zn droplet is consumed or the plasma is not dense enough to produce more ZnO (i.e. the Zn droplet with protruded ZnO NWs exits the plasma plume). Two representative images can be seen in FIGURE 3. The micrographs were taken with a FEI NOVA NanoSEM 600 scanning electron microscope (SEM); the samples were affixed onto a carbon substrate.

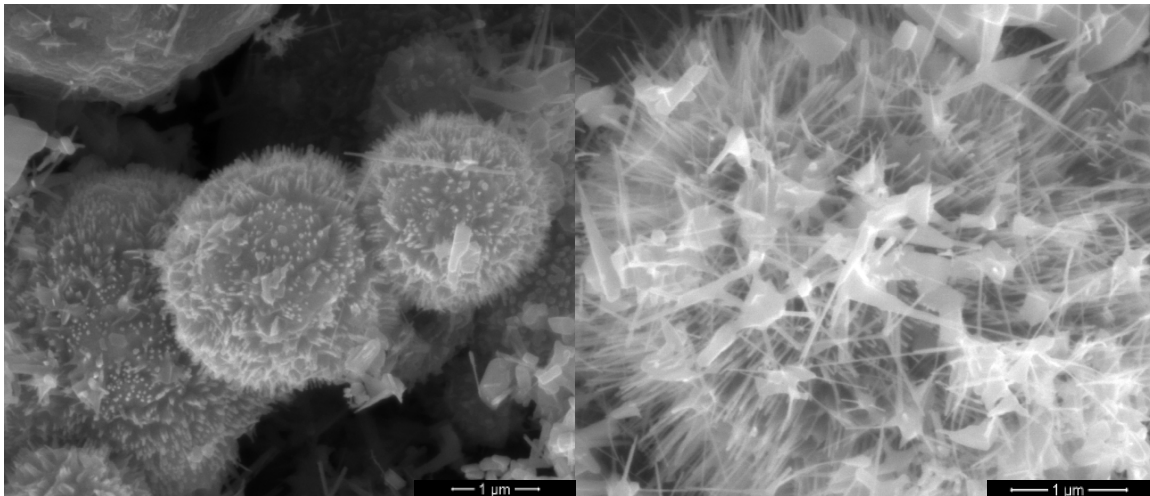


FIGURE 3 – SEM micrographs of ZnO NWs Protruding out of Droplets

The optimized steady state conditions at which the production runs were executed are as follows: one kW power to the magnetron and 15.5 L/min overall gas feed, of which 15% is oxygen and the remainder is nitrogen. The highest quality NWs were collected from the 40 mesh filter at the vacuum pump entrance and from the bottom 65% of the quartz tube which has an inner diameter of two inches and a length of 36 inches.

ZnO NW Purification

Unfortunately, the product is only about 75% ZnO NWs, and the remainder is comprised of un-reacted and partially-reacted Zn NPs and ZnO platelets, ZnO NPs, tetrapods, and various other shapes. Representative images of fresh product ZnO NWs can be seen in FIGURE 4. The wires are up to five microns long, with a diameter ranging from 5 nm to 110 nm (with an apparent mean of about 40 nm).

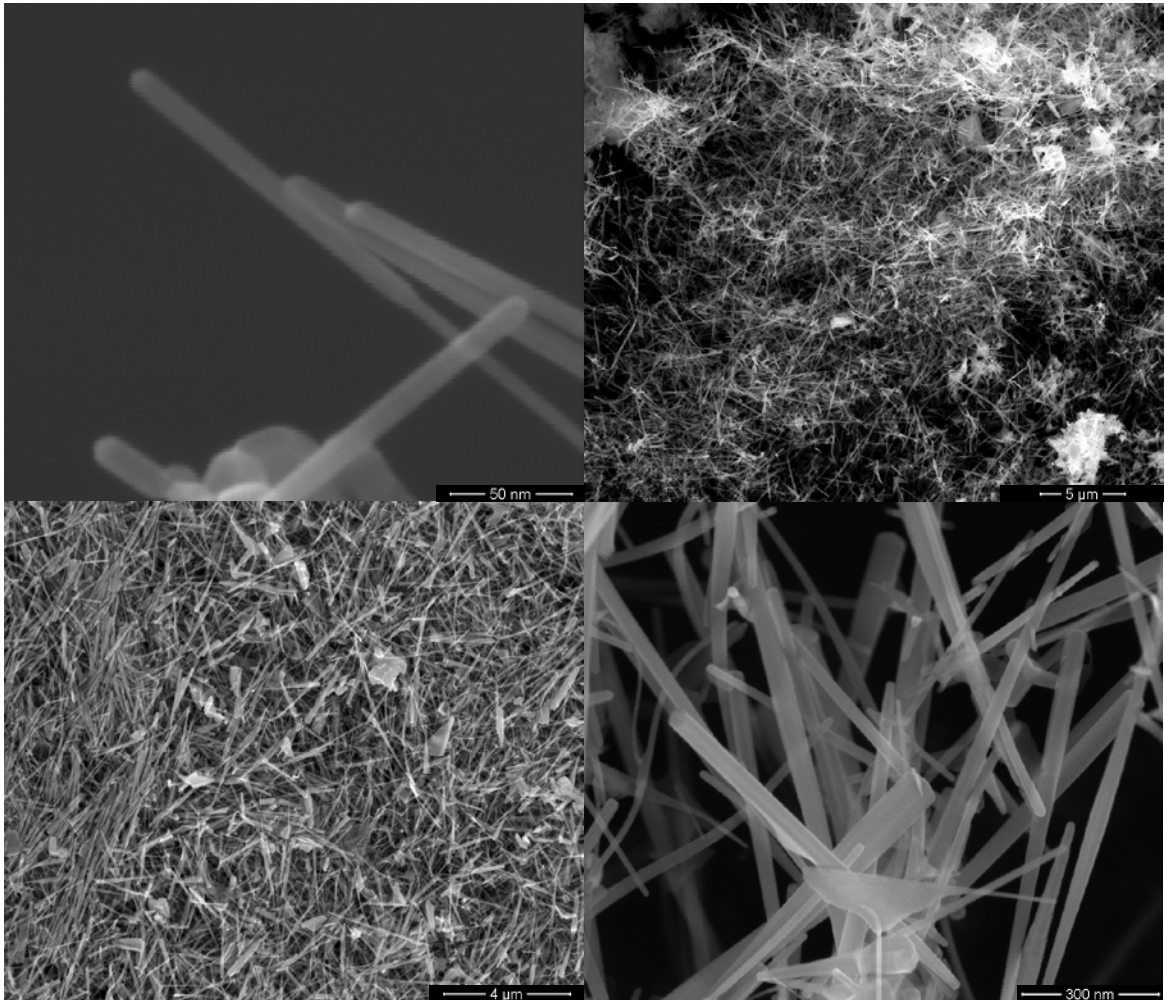


FIGURE 4 – SEM Images of Fresh ZnO NW

To be able to recognize catalyst properties based on the morphology of the ZnO carrier, it is necessary to isolate the NWs from the “junk” particles. Having uniform dimensions would be perfect to study morphology effects; however, given the size heterogeneity of the ZnO NWs and NPs, a separation scheme had to be devised to screen the NWs from the NPs to assure a basic level of shape regularity.

Centrifugation schemes proved to be inefficient and un-scalable. Other schemes, like separation still in flow (based on mass or excitation/charge), were contemplated; but proved difficult to execute. Finally, the elongated shape and single crystalline character of the ZnO NWs proved to be the critical property which allows for separation of ZnO NWs from NPs.

Electro-Kinetic Potential

Zhou (2010) reported that ZnO particle aggregation in suspensions particles with complex morphology or size behave dramatically different from simple (spherical) particles. Electrostatic repulsion of irregular particles can be distinctively manipulated via alteration of pH and particle concentration. To generally test the zeta-potential of ZnO NWs and ZnO NPs, three aqueous solutions with different pH values (6.1, 8.1, and 10.1) were prepared with de-ionized water and either hydrochloric acid or ammonium hydroxide solution. A set of fresh ZnO NW powder and a commercial ZnO NP powder with a particle diameter of 16 nm were put in suspension in the prepared solutions (ZnO ratio = 1:50). Those six suspensions were ultra-sonicated for five minutes in a Fisher

Scientific FS60 ultrasonic bath to assure high initial dispersion of all particles. The zeta-potential of each freshly sonicated suspension was then measured using time-resolved dynamic light scattering via a Zeta Plus Analyzer with a 30 mW solid state 660 nm laser source from Brookhaven Instruments. The six data points are displayed in FIGURE 5.

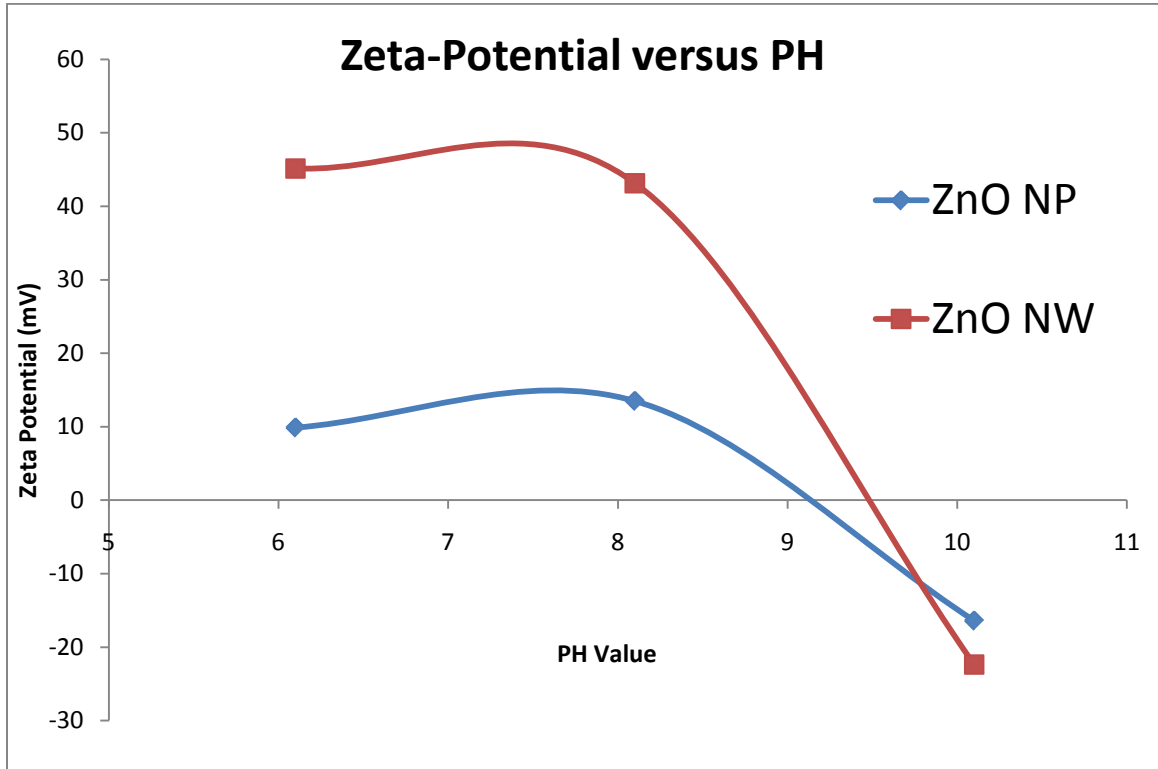


FIGURE 5 – Zeta Potential of ZnO NWs and NPs at Different pH Values

Zeta-potential is a measure of suspension stability. An absolute value greater than 40 mV is considered good stability, an absolute value below 30 mV is considered instable, and an absolute value of 10 mV or below causes rapid coagulation and sedimentation. Based on the results displayed in FIGURE 5, it is obvious that when sufficiently far away from the iso-electric point (IEP), ZnO NWs are significantly more

stable in aqueous suspensions than ZnO NPs. The IEP for both ZnO NWs and NPs remains the same at a pH of 9.2, which is consistent with other publications on ZnO (Degen, 1999), (Andeen, 2005).

A tentative explanation for such a drastic difference in electro-kinetic behavior is the close to perfect single crystalline lattice of the ZnO NWs. Single crystallinity of the NWs with no apparent stacking faults was confirmed by high resolution transmission electron microscopy (HRTEM) on a FEI Technai F20 HRTE-microscope (see FIGURE 6d). The ZnO NW sample was prepared by dispersing the NWs via ultra-sonication in ethanol; dispensing one drop of the suspension onto a carbon-coated copper grid, and letting the ethanol evaporate leaving behind the ZnO NWs. To verify the tagged ZnO NP size, an X-ray diffraction (XRD) pattern was obtained on a Bruker AXS D8 Discover x-ray diffractometer with Ni-filtered Cu- K_{α} radiation ($\lambda = 1.54 \text{ nm}$), employing a scanning rate of 0.05 s^{-1} in the 2θ range from 20° to 89° . The average crystallite size for the commercial ZnO NPs was estimated to be 16 nm, as tagged, by the Debye-Scherrer equation:

$$D_{\text{XRD}} = \frac{\lambda}{\beta \cos \theta} \quad (5),$$

where D_{XRD} is the average crystalline size, λ is the wavelength of Cu- K_{α} x-rays, β is the full width at half maximum (FWHM) of the most prominent diffraction peak, and θ is the Bragg's angle. At such a small size, the NPs could not be dispersed down to single crystallites without the help of some strong surfactant. SEM images show that a fresh

sample of the NPs consists of sphere-like agglomerations with 300 nm and up to 10 μm in diameter (see FIGURE 6). Large amounts of randomly oriented small crystallites are stacked into bulk particles. Consequently, the bulk particles' net surface charge is smaller due to cancelations between different crystallites attached to each other. The ZnO NWs, however, express undisturbed surface charges due to perfect alignment of the crystal lattice in a single crystal bulk particle (i.e. NW). This makes it more difficult for the particles (i.e. NWs) to overcome the electrostatic repulsion between each other; thereby evading agglomeration which stabilizes the suspension.

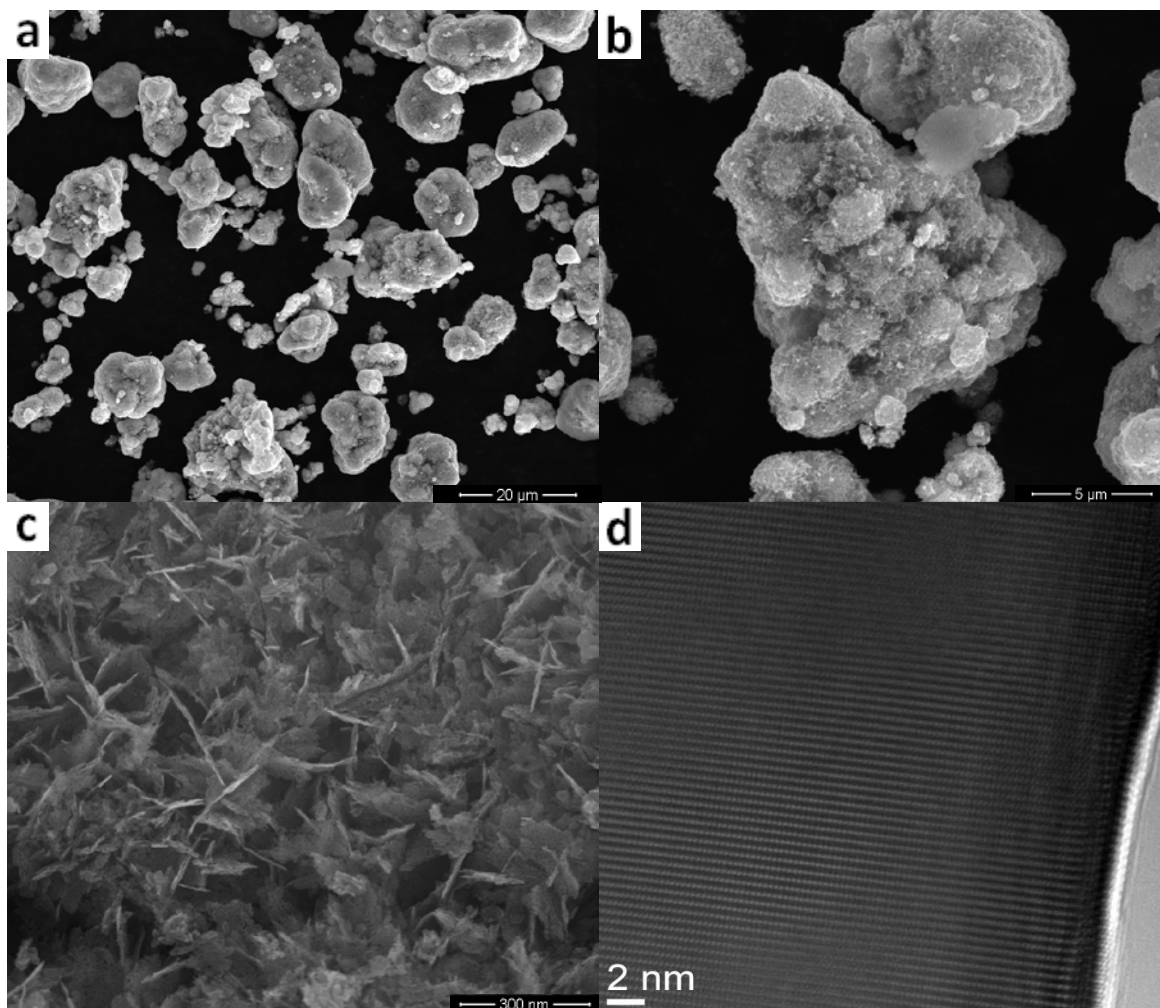


FIGURE 6 –Representative SEM Images of Commercial ZnO NPs (a, b, c) and HRTEM Image of a ZnO NW (d) with Incident Electron Beam along $\{2\bar{1}10\}$ Direction

Separation Procedure

Two simple formats to separate the NWs from the NPs and junk particles come to mind which utilize the substantial difference in suspension stability. One is to suspend the mixed ZnO NW/NP in de-ionized water (pH = 7) in an ultra-sonic bath. After some time, for which an optimum can be found by trial and error, the supernatant is separated from the precipitate via simple extraction. With the help of a base, the pH value of the solution is then increased to around the IEP, which causes the NWs to drop out of suspension. The clear (basic) solution is then extracted and the bottom cake is collected. Alternatively, one could filter the NWs with a micro-pore filter instead of applying a base.

Examination of Suspension Behavior

Two suspensions (one with ZnO NPs and one with freshly-produced, mixed ZnO NWs) were prepared with de-ionized water in an ultra-sonic bath. Once the NPs and mixed NWs were well dispersed, the suspensions were taken out of the sonicator. The vial with the ZnO NPs cleared up completely after ten minutes and the white NPs amassed at the bottom. The second vial with the mixed ZnO NWs also developed a small bottom deposit but stayed otherwise murky for days. A sample was taken from the supernatant of the second suspension, which was aged for 20 minutes. Another sample was also taken from the corresponding sediment. The bottom deposit seemed to consist of NPs, various other irregularly shaped particles, and a few NWs (see FIGURE 7 a, b). The

suspension, on the other hand, appeared to be almost entirely made up of ZnO NWs, with a few elongated platelets in-between the bulk congregation of ZnO NWs (see FIGURE 7 c, d). Overall, the NW fraction of the fresh ZnO NW mix was increased from about 75% to about 95%, which denotes an enormous boost in shape uniformity.

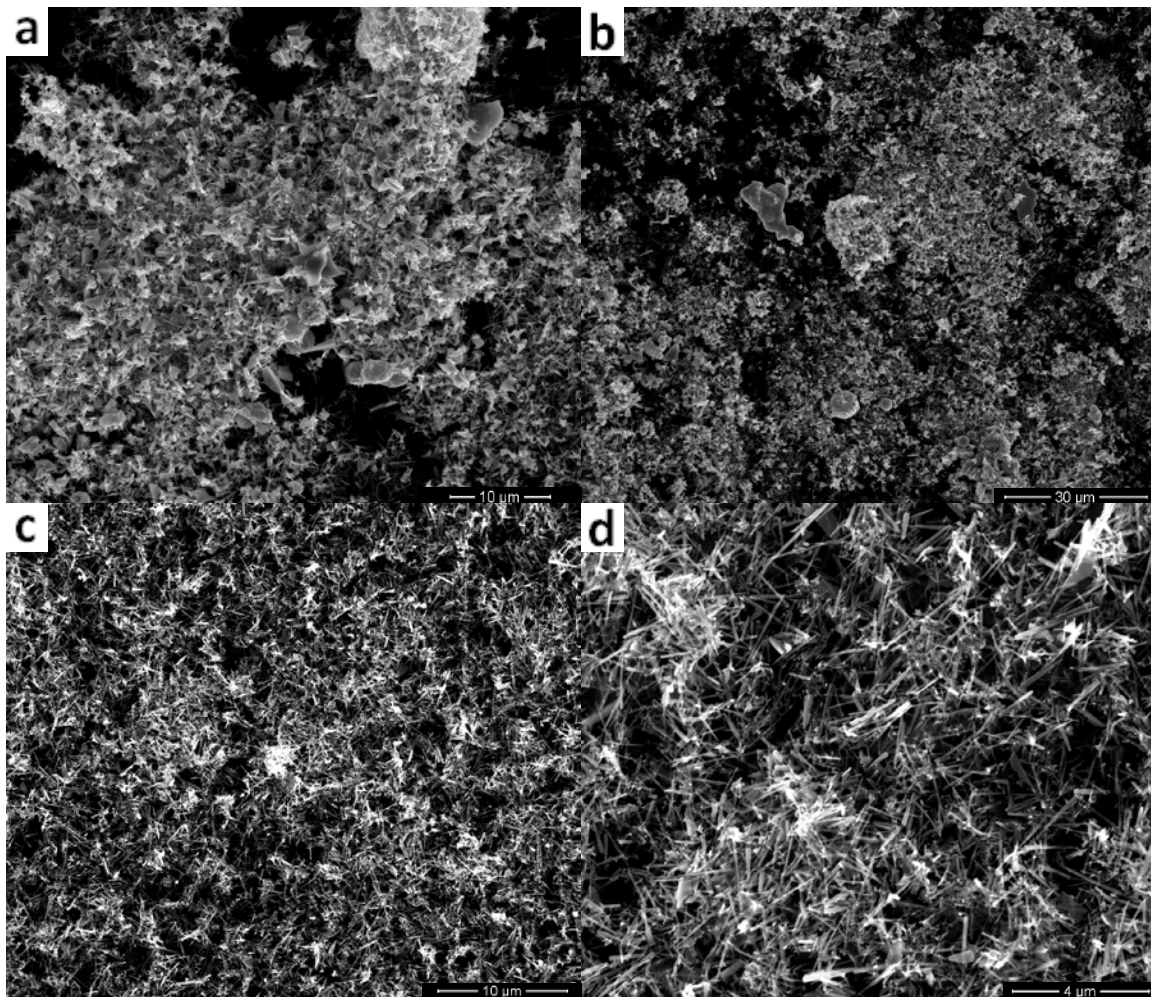


FIGURE 7 – ZnO Junk-NPs from Bottom Cake (a, b) and ZnO NWs from Suspension (c, d)

A sample of purified ZnO NWs was checked for its surface area via the Brunauer-Emmett-Teller (BET) method using nitrogen at 77K on a vacuum volumetric gas-sorption

Micromeritics TriStar 3000. The result of 20 m²/g is in agreement with other publications and simple geometric estimations (see TABLE III in the Appendix).

III. CATALYST PREPARATION AND CHARACTERIZATION

With a reasonable supply of ZnO NWs at hand, preliminary trials were conducted to develop an understanding of and select practical methods by which to deliver the active nickel phase onto the ZnO NWs. Unfortunately, the thermodynamics for ion-exchange are not favorable for the Ni/ZnO system. Consequently, efforts to achieve a thin or partial nickel coating onto the ZnO NWs were eventually abandoned. An attempt to disperse Ni NPs onto ZnO NWs during the production step in the plasma plume was made, but only delivered bare ZnO NWs with cubic NiO crystals loosely scattered around the NW congregation. Using an organic nickel salt instead of Ni NPs during the NW production step could possibly disperse small Ni NPs onto the ZnO NWs. This approach, however, appears risky and could damage the feeding system or cause undesirable NW quality due to the introduction of new gas species. Nevertheless, one such attempt will be conducted in the future and thoroughly characterized. Other relevant approaches like galvanic and also electro-less plating with a variety of reducing agents were contemplated; however, deterred by further equipment and materials costs, the approach was discarded for immediate exploration. The idea holds enough promise, though, as one could potentially have full control over the extent of nickel loading by

simply manipulating timing and concentrations. Given the budget and time constraints, impregnation with nickel solutions was chosen as the method suitable to deliver and test a first product.

Choice Of Nickel Salt

There are several nickel salts which lend themselves to being used as the impregnation precursor. The opening selection criteria were hazardousness, solubility, cost, decomposition temperature, and hazardousness of decomposition product gases. Nickel nitrate hexahydrate and nickel acetate tetrahydrate (NiAc) were the final candidates, of which the acetate was chosen due to its relatively benign decomposition product gases (De Jesus, 2004).

TGA/DSC Decomposition Temperature And Nickel Wetting

A ZnO NW sample was impregnated with an aqueous NiAc solution. The Ni to ZnO ratio was 20 wt% and the pH of the solution was kept at nine with the help of ammonium hydroxide. The solution water of the sample was slowly evaporated in a furnace at 110°C and the dry sample was collected. To expose the decomposition temperature of the acetate portion, a thermal gravimetric analysis (TGA) with differential scanning calorimetry (DSC) was conducted in ambient atmosphere on a Netzsch STA 409C. The TGA curve (see FIGURE 8) shows that water is released

continually to about 300°C with a small evaporation spike around 210°C, as indicated by an endothermic event at that temperature. The acetate begins to slowly pyrolyze at around 300°C and is dramatically and completely consumed by 340°C, as indicated by the intense exothermic event, with a peak at 338°C. A second sample with the same Ni to ZnO ratio was prepared by simply mixing the dry powders together adding no water or base at all. The TGA curve for the dry sample shows complete water loss by around 125°C. There is no activity from 125°C to around 300°C, at which point the acetate starts decomposing again in the same manner as the first wet sample. The gradual loss of water for the first sample as compared to the second dry powder sample indicates increased interaction between the ZnO NW carrier and the nickel solution. This shows promise of nickel being intimately contacted to the ZnO NWs.

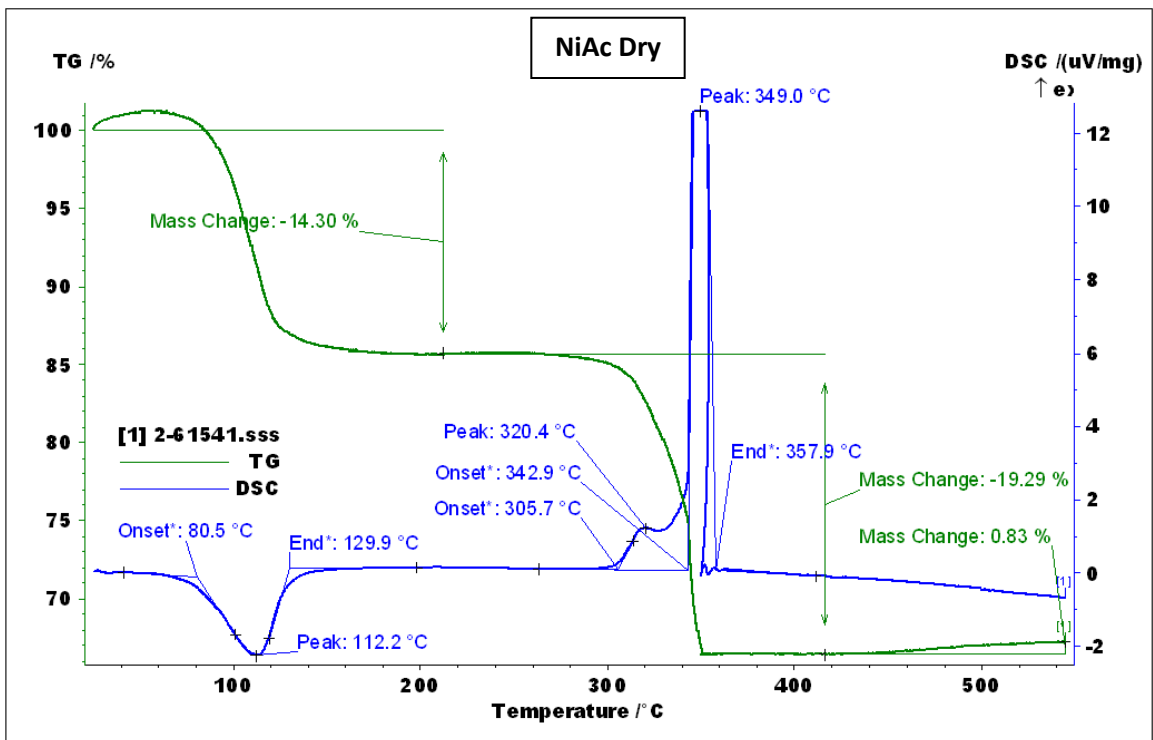
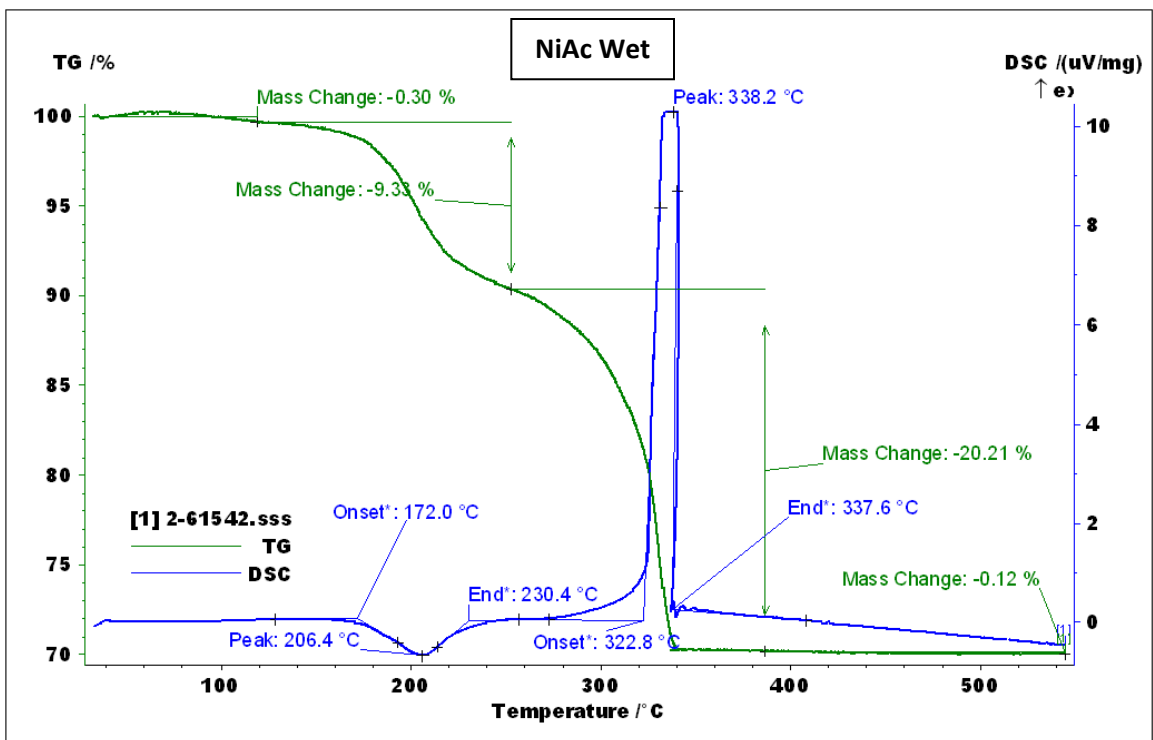


FIGURE 8 – TGA/DSC Curves for NiAc Decomposition on ZnO NWs

Phase Identification Of Calcined Product Via XRD Signatures

In order to identify the desired phases of the calcined product, a ZnO NW sample was impregnated with 30 wt% NiAc (as described previously) and caclined in air for two hours at 400°C. The calcined powder was loosely crushed in a mortar for XRD analysis. The XRD pattern shown below in FIGURE 9 precisely displays the characteristic signature peaks of hexagonal wurtzite ZnO and face-centered cubic bunsenite or NiO. The NiO peaks appear fairly broadened, which indicates a small crystallite size. As expected, the mean particle size calculated from the Debye-Scherrer equation came to about 11 nm. Aside from identification of the two desired phases, the nickel loading was also confirmed to be 30.1% NiO.

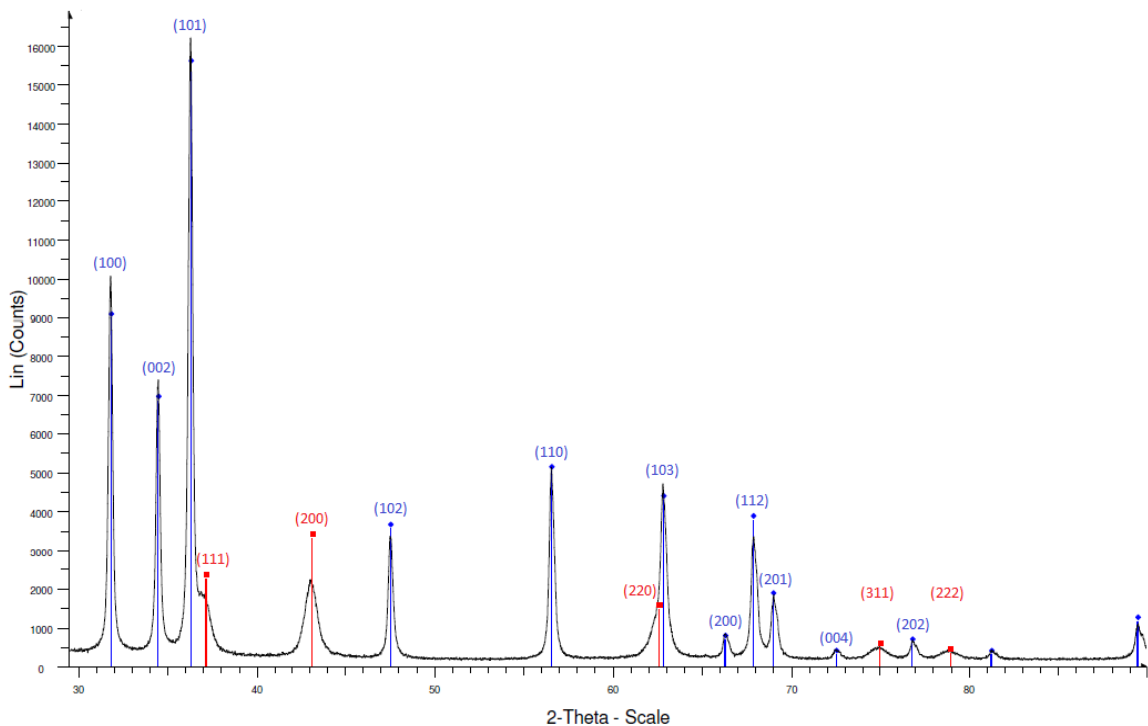


FIGURE 9 – XRD Patterns of Hexagonal Wurtzite ZnO (blue) and Face-Centered Cubic Bunsenite (red) Phases with Plane Indices

Morphology Assessment Via SEM

Considering the dimensions of the ZnO NWs, the NiO particles were expected to be a bit smaller to fit tightly onto and in-between the NWs. The nickel loading of 30% simply appeared to be too high for the NiO particles to be well-dispersed. As confirmed by SEM and TEM runs, the NiO particles nucleated on ZnO NW surfaces but also on other already existing NiO sites into larger clusters (see FIGURE 10). There was simply not enough interfacial legroom for a thin coating of NiO NPs. To avoid nickel overloading and to keep ZnO sites accessible, a favorable loading ratio of 15% nickel was estimated based on a 50% ZnO NW coverage (see TABLE III in Appendix).

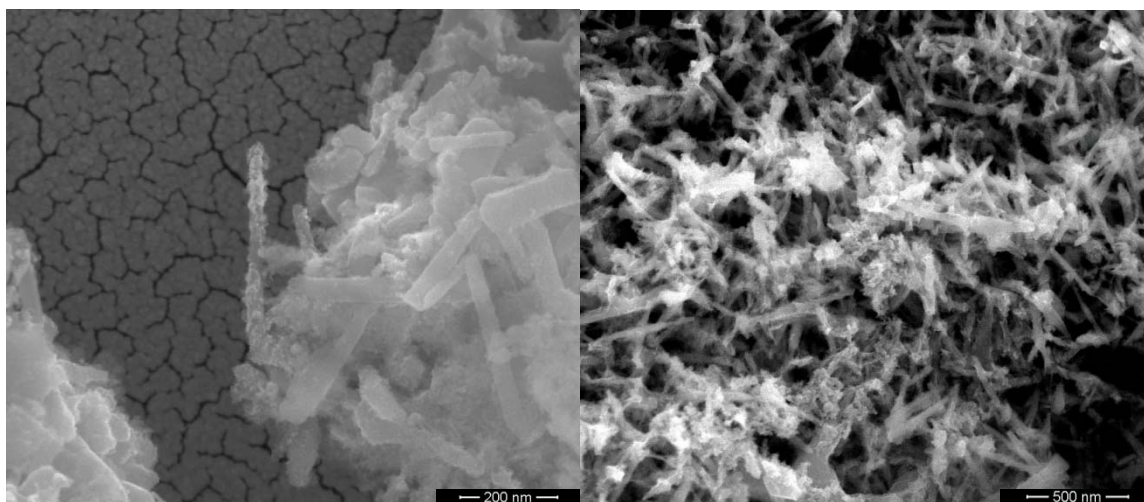


FIGURE 10 –SEM Images of Calcined ZnO NWs with 30% Nickel Over-Loading on a Gold-Coated Quartz Substrate

TEM And EDS Mapping Of Individual ZnO NW

In order to see how the nickel distribution improves with 15% loading, a sample was prepared and inspected via TEM (see FIGURE 11). It can be speculated that the Ni NPs, which are not firmly affixed to ZnO NWs; but rather loosely scattered around, were detached from the wires when the sample was ultra-sonicated for about ten minutes. Close-up images of NiO NPs that were affixed to ZnO NWs appeared to hold well. Complementary confirmation of the ZnO and NiO phases is provided by selected area electron diffraction which, not surprisingly, also reveals hexagonal wurtzite and bunsenite.

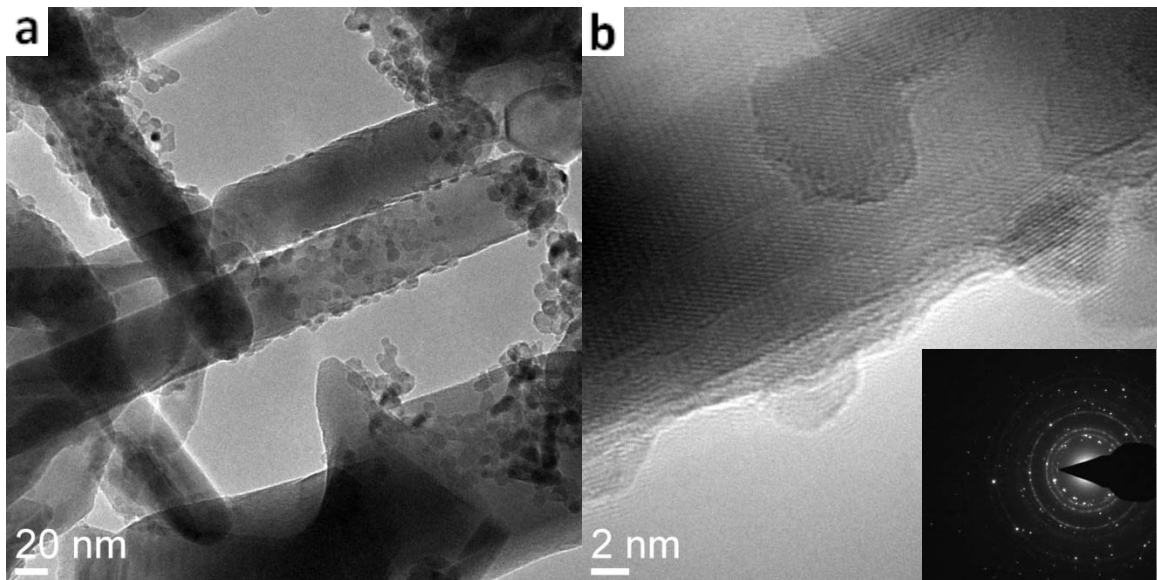


FIGURE 11 – TEM of NiO NPs Affixed to and Detached from ZnO NWs (a), HRTEM Close-Up and Selected Area Electron Diffraction (b)

To identify elemental composition and confirm yet another way that the NPs decorated onto the ZnO NWs are indeed NiO, an energy-dispersive x-ray spectroscopy (EDS) map was generated for an area of and surrounding a single NW. The individual elemental maps, which are displayed in FIGURE 12, unmistakably show how nickel is distributed in a manner resembling particles and particle clusters over the NW.

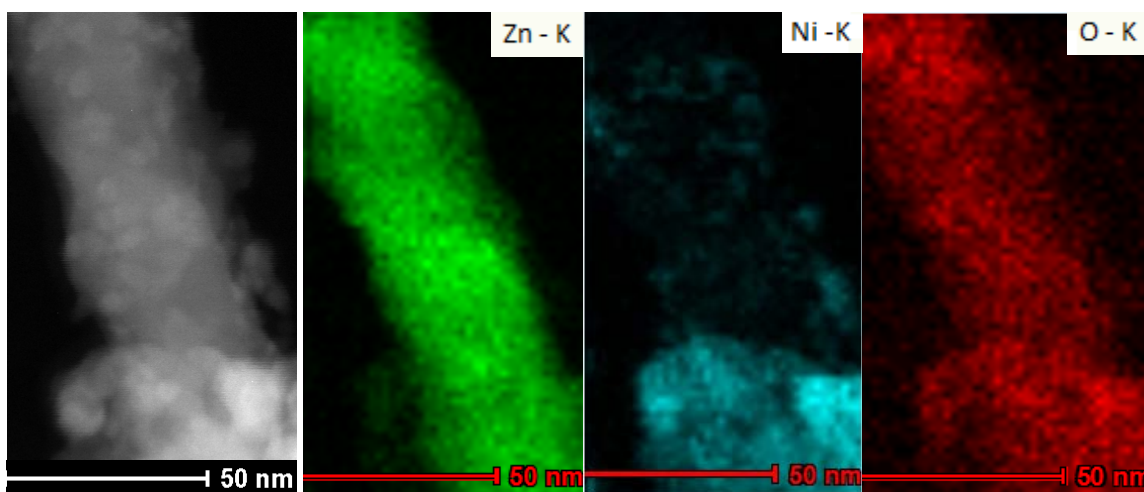


FIGURE 12 – HRTEM Image and EDS Maps of a Single NW for Individual Elements

TEM In-Situ Decomposition Of NiAc On ZnO NWs

Another TEM run was carried out to expose whether the loosely scattered NiO NPs nucleated on the spot, independently of the wires, or were disconnected from the ZnO NWs during sample preparation (i.e. sonication). A ZnO NW sample was prepared without calcination; a drop of the ZnO NW/NiAc suspension/solution was dripped onto a carbon grid, dried, and loaded into the TEM. A prior SEM run on the same sample revealed a reasonably even distribution of the NiAc salt alongside the ZnO NWs (FIGURE

13). The sample in the TEM chamber was slowly heated to 330°C as a result of which nickel nuclei started to emerge from the amorphous NiAc. All images in FIGURE 14 were recorded at a final temperature of 430°C. The chamber was under high vacuum which prevented formation of NiO. Upon comparison of several different sample regions before and after in-situ calcination, it appears that nickel nucleates indiscriminately on any interface present; this also includes the carbon grid. Overall, nickel dispersion is very high with very few and small agglomerations. The nickel particle size averages around 30 Å, which is an excellent result and a good indicator for high catalytic activity.

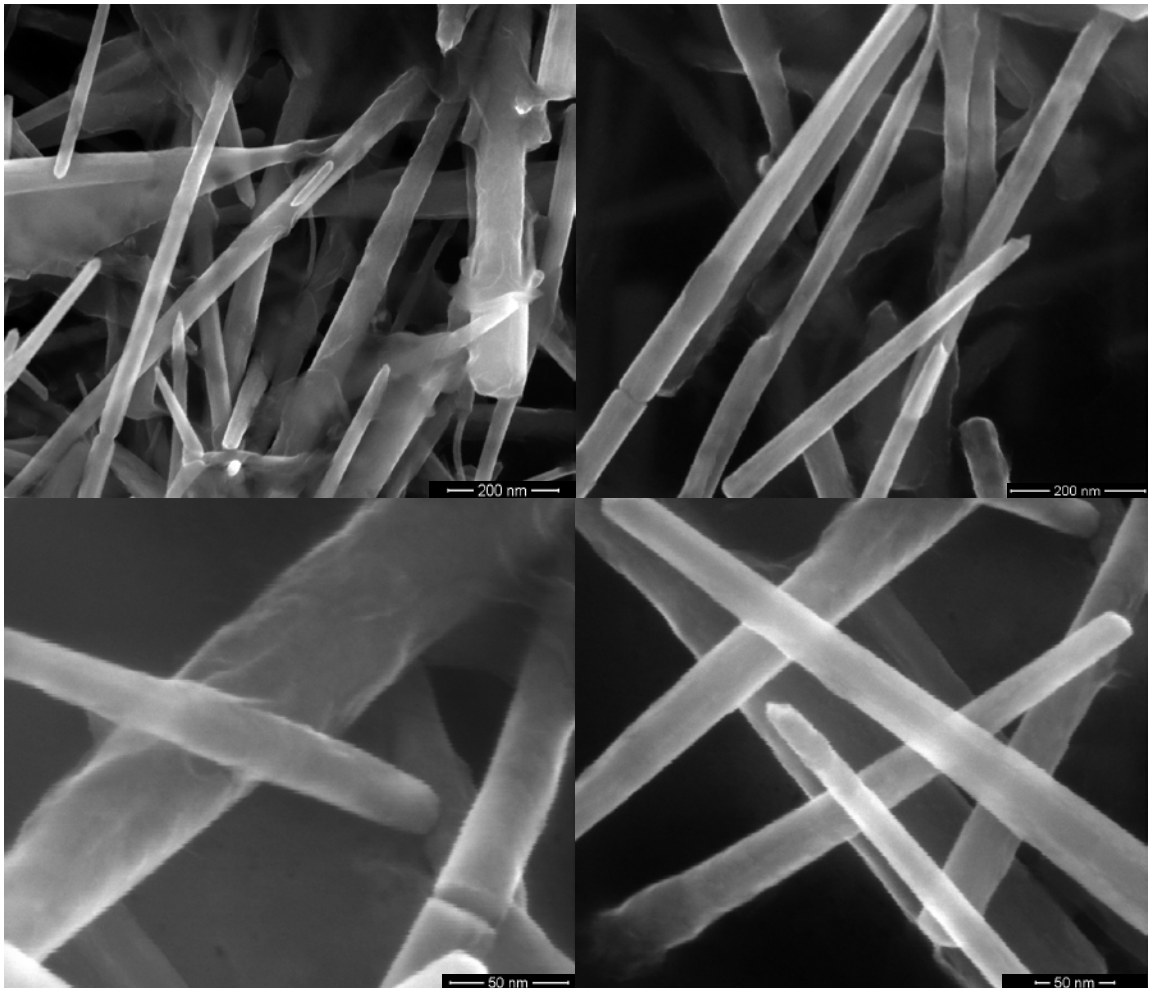


FIGURE 13 – Representative SEM Images of ZnO NWs Coated with NiAc

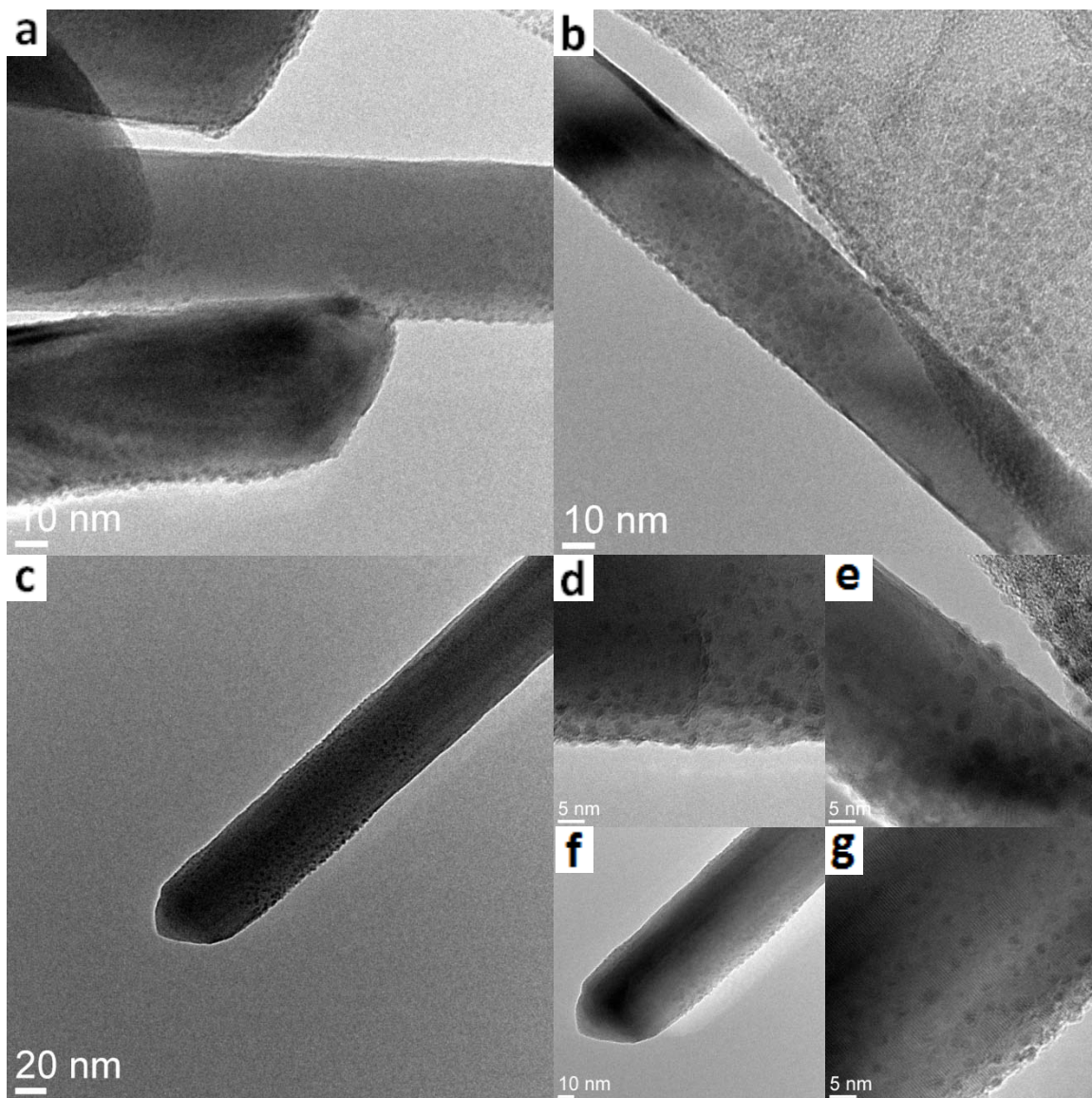


FIGURE 14 – TEM Images of In-Situ Calcined NiAc on ZnO NWs (a, b, c), Images (d) and (e) are Close-Ups of (a) and (b), (f) is a Close-Up of (c), (g) is a Close-Up of (f)

Analysis Of NiO NP – ZnO NW Interaction Via TPR And Hot Stage XRD

To test the sintering susceptibility of the NiO/ZnO NW system during reduction, two time programmed reduction (TPR) runs were conducted on NiO decorated ZnO NWs and on commercial ZnO NPs. The two samples were loaded with 20% nickel and reduced in a nitrogen stream with five percent hydrogen on a Micromeritics Autochem II 2920. The ramp rate of the reduction was ten degrees per minute and the hydrogen consumption signal was recorded from 30°C to 500°C. Both TPR profiles (see FIGURE 15) display one major peak which points to a relatively uniform nickel particle size distribution in the sample. The ZnO NP sample has a reduction maximum of around 345°C and the ZnO NW sample at 358°C. The considerable difference between the reduction maxima implies that the NP sample with the lower reduction temperature shows relative ease of NiO reduction compared to the NW sample. Reducibility can serve as a measure of nickel-support interaction. The stronger the NiO interacts with the ZnO support the more difficult it is to reduce it to nickel. The stronger metal-support interaction is also related to smaller NiO and nickel particle sizes.

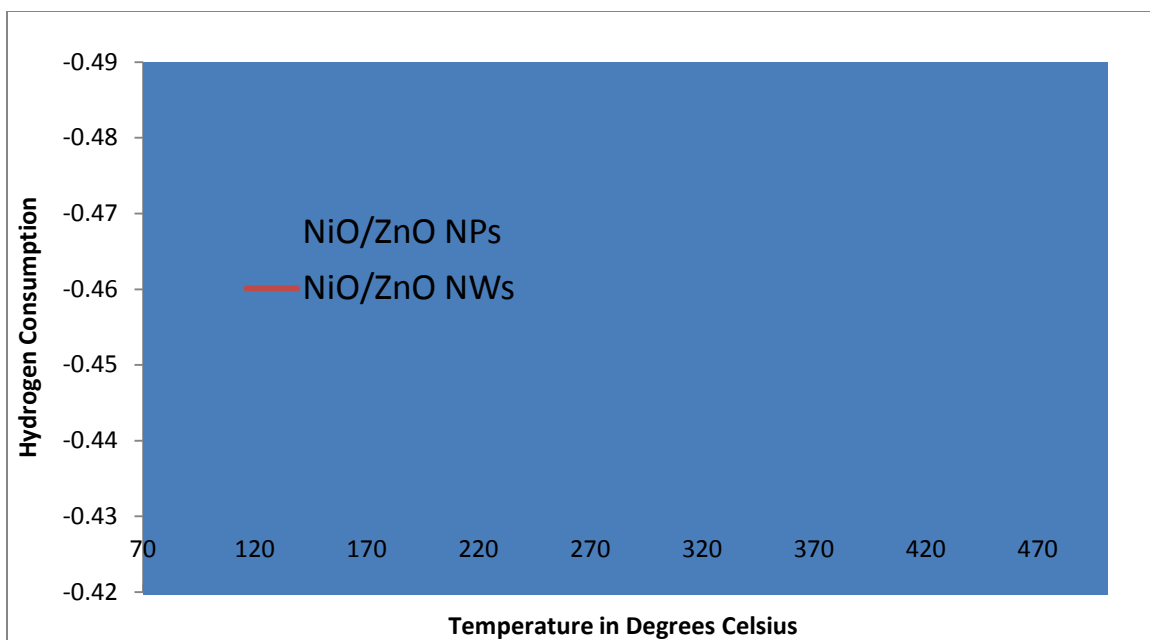


FIGURE 15 – TPR Curves for NiO on ZnO NPs and ZnO NWs

To gain insight into the nickel particle size evolution during reduction, a hot stage XRD reduction was conducted. Unfortunately, a ZnO NW sample with low (25%) NW ratio was used for this experiment; therefore, the experiment will have to be repeated in the future. For the current data, an XRD profile was recorded for every 25°C increase in temperature with the same reduction conditions as the TPR runs. When the ZnO NP sample (which was reduced in the same manner) is taken as a reference, the ZnO NWs appear to reduce the extent of nickel sintering. FIGURE 16 displays the mean crystallite size evolution during reduction of both nickel decorated ZnO NPs and ZnO NWs.

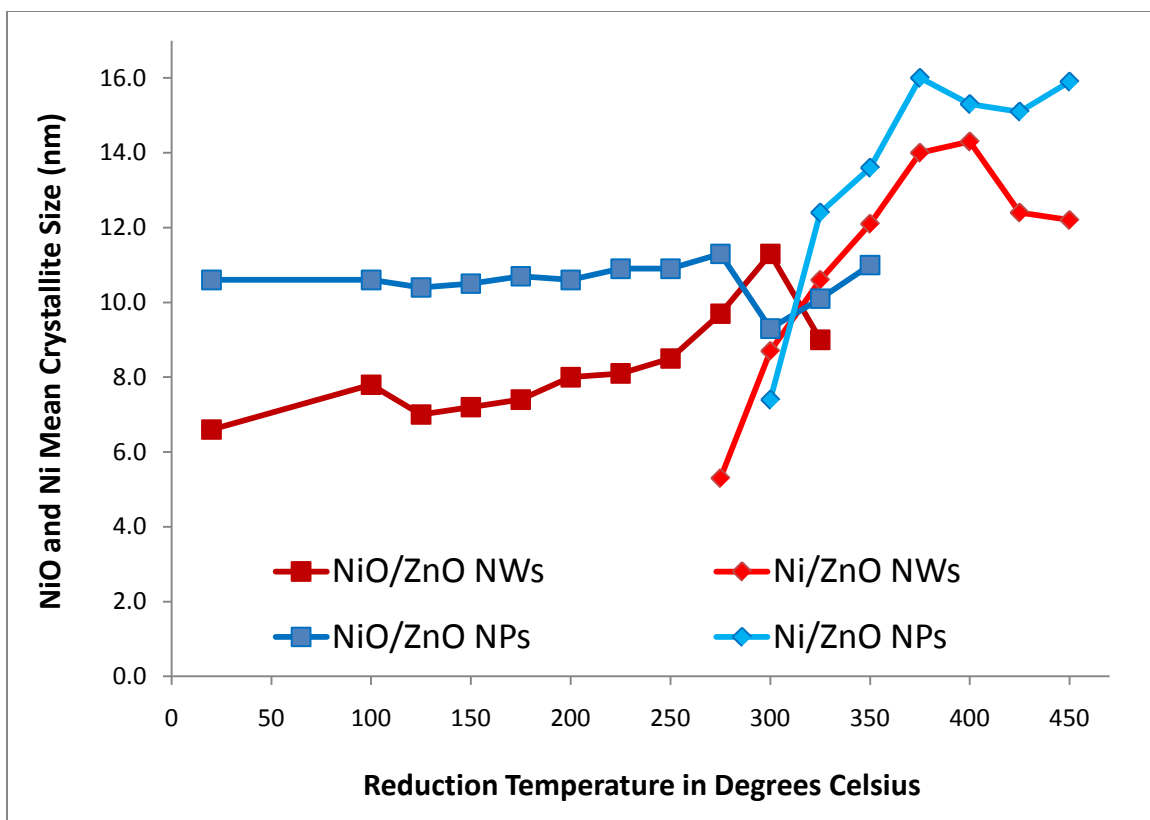


FIGURE 16 – Mean Crystallite Sizes of Nickel on ZnO Carriers from Hot Stage XRD Data

Sulfur Uptake Confirmation Via XRD

To practically investigate if the proposed catalyst carrier chemisorbs and stores hydrogen sulfide (H_2S), a ZnO NW sample of 0.2 g was mixed into a slurry with ethanol, spread onto a quartz plate, and placed in a vacuum reactor chamber. The reactor was slowly pumped down to a moderate 0.05 torr and heated to 200°C. A 25 sccm stream of H_2S was then flown over the sample for 14 hours. As shown in FIGURE 17 below, XRD analysis identified a cubic zinc sulfide (ZnS) phase. Quantification revealed that 38.2% of the sample is ZnS, and the 61.8% remainder is comprised of ZnO.

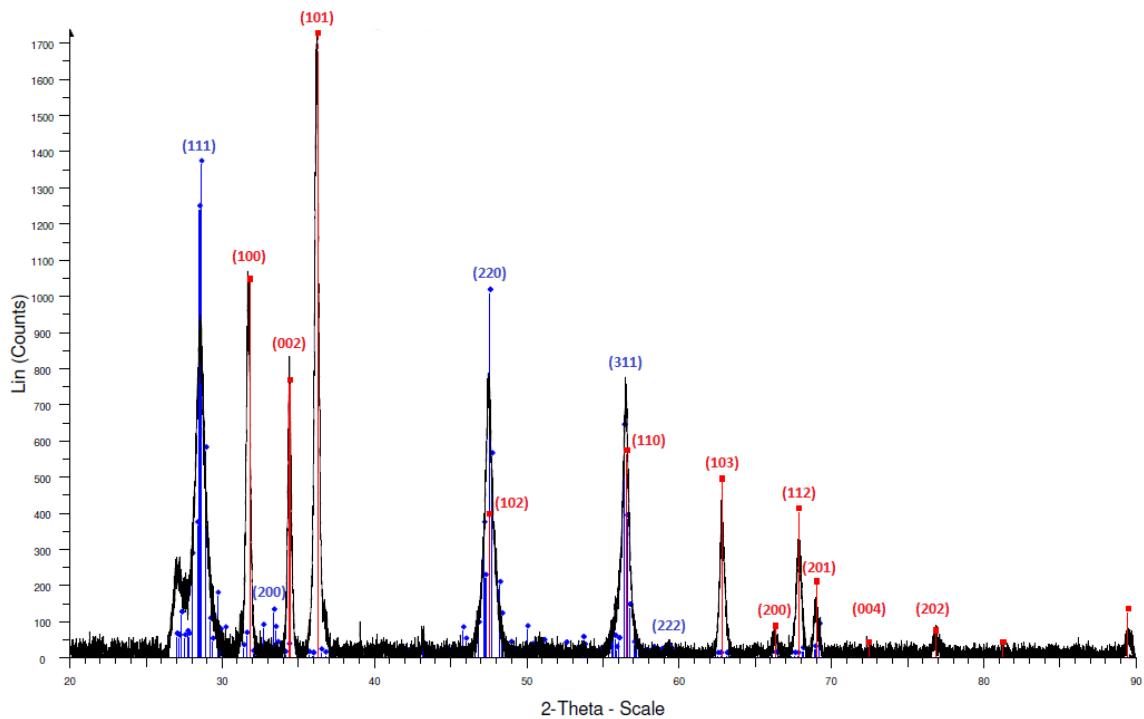


FIGURE 17 – XRD Patterns of Hexagonal ZnO (red) and Cubic ZnS (blue)

Now that the ability of ZnO NWs to store sulfur was demonstrated it was necessary to assess how this affects the morphology of the NWs given the lattice mismatch between both phases. As shown in FIGURE 18, SEM images of the sulfided sample appear to show “swelling” of the NWs; however, the general morphology is well maintained.

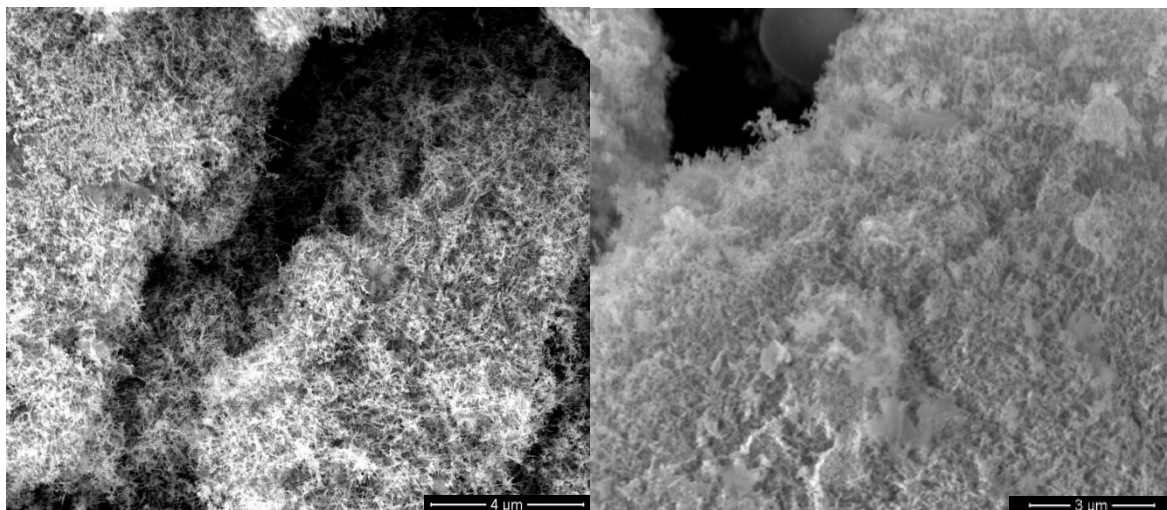


FIGURE 18 – Representative SEM Images of ZnO NWs after Exposure to H₂S

Crush Strength Test Of Catalyst Extrusions

The general vehicles with which to deliver catalytically active phases in industrial arrangements are either extrusions or tablets. Extrusions are made by pressing product dough through commonly circular templates. There are several lubricants and binders mixed in with the carrier dough. The exact binder compositions depend on the materials used and are highly protected trade secrets as they can significantly improve crush

strength and surface area. Most commonly, binders are comprised of alumina or silica phases with small amounts of various clays.

To be able to test the proposed catalyst in standardized reactor units, it needs to be expressed in extrusions. Unfortunately, small industrial and even funnel extruders waste a lot of material per run. Therefore, a syringe was used to hand-extrude the catalyst for all extrusion trials. Actual photographs of the extrusion process are attached in the Appendix. A few sample extrusions with varying ratios of Ni, ZnO, and α -alumina were produced (extruded, dried, calcined) and tested for crush strength with a Mecmesin compression strength tester. In comparison to industrial requirements, there is a lot of room for improvement as the results only ranged from 0.3 to 0.85 lb/mm. A rule of thumb is that crush strength should be at least one lb/mm to be suitable for standard testing procedures. Given the time constraints, it was necessary to proceed and test the final extrusions anyway, rather than finding better binding materials and/or composition ratios.

Final Catalyst Preparation

The proceeds of several ZnO NW production runs were collected (10.28g) and suspended in a one liter beaker filled with de-ionized water. After a 15 minute treatment in an ultra-sonic bath, the suspension was allowed to settle for 20 minutes before the supernatant was vacuum-filtered through a paper filter with a 2.5 micron pore size. The filter with the attached wet filter cake was dried for one hour at 110°C,

after which the dry ZnO NWs were collected from the filter. The final yield of high purity ZnO NW was 70% or 7.2 grams.

For an intended final weight composition of 64:20:16 (ZnO: Al₂O₃: Ni), 5.84 grams of the high quality product was mixed with 1.82 grams of γ -alumina and 6.35 grams of NiAc. The product mixture was suspended in 250 ml of de-ionized water and was ultra-sonicated for about eight minutes to re-disperse the ZnO NW filter cake flakes. The beaker with the pale green suspension was put in a furnace at 80°C over night. Once 150 ml of water were evaporated, the resulting creamy substance was further heated to 150°C with occasional stirring. The final 30 to 40 ml were thick enough to extrude the dough into extrusions, which were then dried over night at 70°C. The final drying temperature was ramped up to 250°C at one degree per minute. The product extrusions became darker but stayed greenish until they were calcined at 400°C for two hours, at which point they almost immediately turned into a dark grey. After a cool-down period, the extrusions were sized to five by two millimeter pieces of which 10 ml were measured out for testing.

IV. ACTIVITY AND HYDRODESULFURIZATION TEST

To examine the final catalyst extrusions for desulfurization activity and capacity, they must be exposed to a model hydrocarbon stream spiked with an assortment of aforementioned “difficult” aromatic sulfur species in a setting that closely resembles industry conditions. It seemed appropriate to employ a diesel feed that contained aromatics to see if the catalyst also conveyed an appropriate level of regular hydrogenation activity.

Feed Composition

A standard diesel feed was acquired from Exxon containing 25% of various aromatic and poly-aromatic compounds. The sulfur content of 20 ppm consisted mostly of thiophene (10 ppm), benzo-thiophene (3 ppm), di-benzo-thiophene (3 ppm), and a few moderately and severely sterically hindered di-benzo-thiophenes.

Reactor Loading

The 2.21 X 80 cm packed bed reactor-tube employed for the activity test was loaded according to the specifications in TABLE IV. A schematic of the reactor tube is displayed in FIGURE 19. A unit diagram (FIGURE 24) and an actual photograph of the reactor can be seen in the Appendix.

TABLE IV

REACTOR LOADING SPECIFICATIONS

Material	Quantity
Glass Wool	2 g
Glass Beads	15 cm ³
Silicon Carbide	108 g
Cat. Extr. + SiC	3 aliquots
Glass Wool	2 g
Cat. Extr. + SiC	4 aliquots
Glass Wool	2 g
Cat. Extr. + SiC	3 aliquots
Silicon Carbide	72 g
Al ₂ O ₃ Extrusions	15 cm ³
Glass Wool	2 g
Aliquot = 7.2g SiC + 1.06g of catalyst extr.	

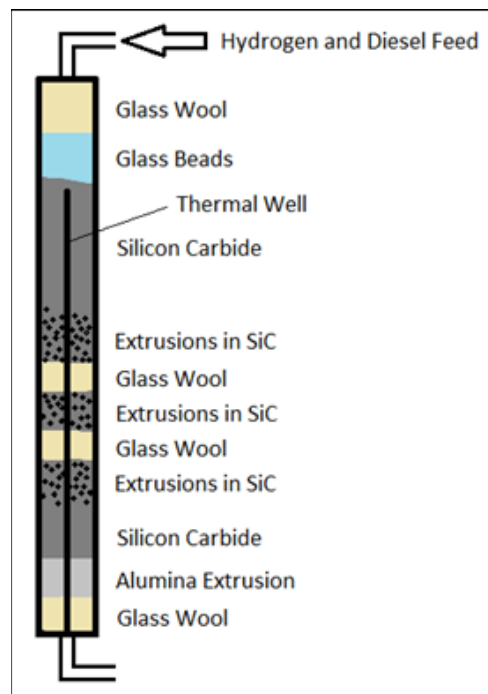


FIGURE 19 – Reactor Schematic

Activity Test

Once the reactor tube was fully loaded and connected, it was purged in a nitrogen flow for 30 minutes. To reduce the NiO particles to metallic Ni, one liter per minute hydrogen was flown over the bed at 430°C for 16 hours. In retrospect, considering the Hüttig temperature, the reduction temperature chosen was probably too high for optimal results and the reduction stage too long. Before the pump for the diesel feed was started, the five reactor heater zones were programmed to fire at 190°C. The mass flow meter for the hydrogen was reduced to 0.098 liters per minute at 435 psig. The diesel pump rate was set to 0.5 ml/min, which, relative to the superficial volume of the catalyst extrusions (10 ml), translates into a liquid hourly space velocity (LHSV) of 3 h⁻¹. Product samples were collected every four hours.

Aromatics Breakthrough

The first two days worth of product samples were tested for aromatics content with a Lambda2 UV/VIS spectrophotometer from Perkin-Elmer. All freshly collected samples were twice diluted with iso-octane (2,2,4-Trimethylpentane) before they were analyzed. The background points were assessed at 246 and 310 nm, and the peak point was measured at 270 nm. All values are listed in TABLE V in the Raw Data section.

To provide a standard against which one can assess the performance of the Ni/ZnO NW/Al₂O₃ catalyst, the aromatics data curve was displayed with two other commercially researched catalyst samples (see FIGURE 20). The two catalysts chosen for

display were previously run in the same test unit at the same operating conditions. The first choice is the best available nickel-alumina catalyst (>55% Ni), hereafter referred to as catalyst “best”, which is not commercially sold, as it is not price-competitive and is also too weak (low crush strength). The second choice is also a nickel-alumina hydrogenation catalyst, hereafter referred to as catalyst “weak”, which is commercially available but represents the end of the performance spectrum.

As is plainly evident, the first trial with Ni/ZnO NW/Al₂O₃ loses aromatics hydrogenation activity very rapidly. The feed aromatics content practically breaks through after one day on stream.

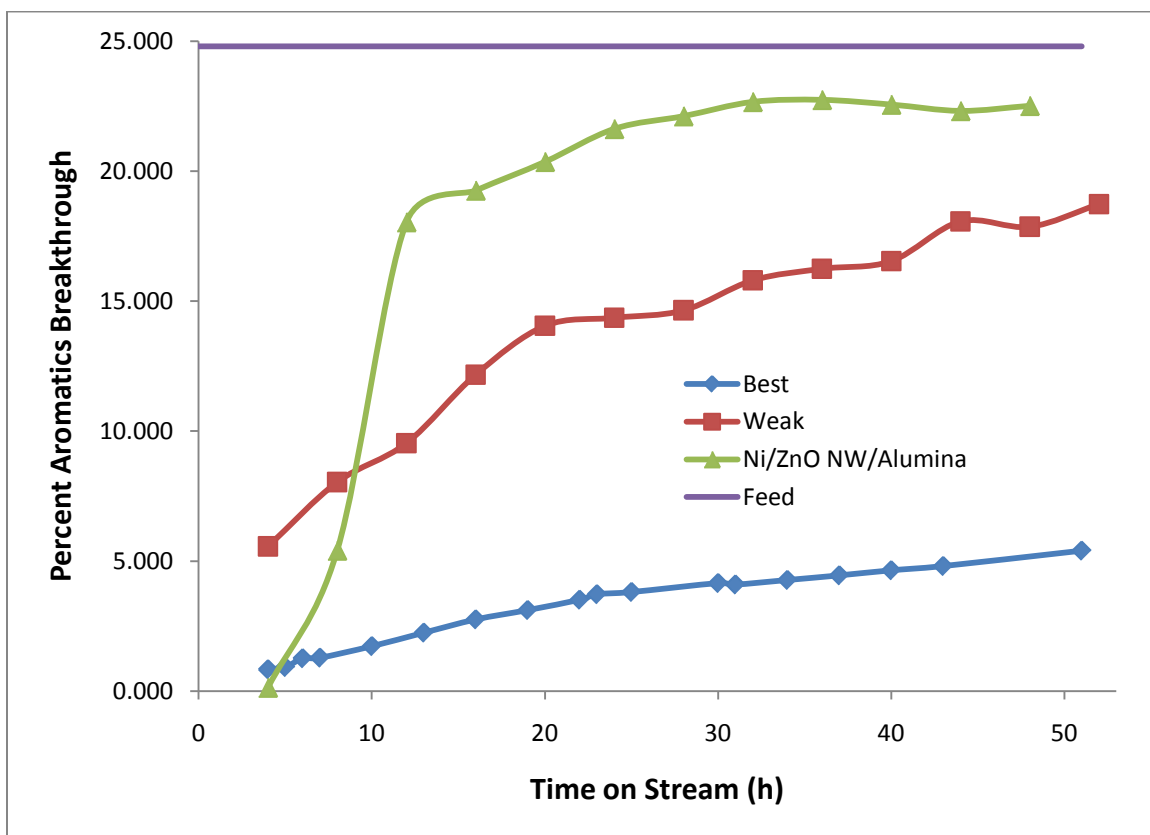


FIGURE 20 – Aromatics Breakthrough of Two Commercial Catalysts and Ni/ZnO NW/Al

Sulfur Breakthrough

The sulfur content in the product samples was analyzed with an Antek 9000 elemental sulfur analyzer and was also compared to sulfur data of older runs. The sulfur uptake capacity of the Ni/ZnO NW/Al₂O₃ catalyst looks at least encouraging (see FIGURE 21). Sulfur in organic sulfur species needs to be catalytically converted to H₂S in order for it to be stored in sulfide form in the catalyst/adsorbent. The fact that there is very little sulfur in the product initially reveals that the Ni/ZnO NW catalytically breaks down the sulfur into H₂S which is then adsorbed by the ZnO NWs. Even though the performance is inferior to conventional catalysts, the concept of reactive adsorption was likely demonstrated.

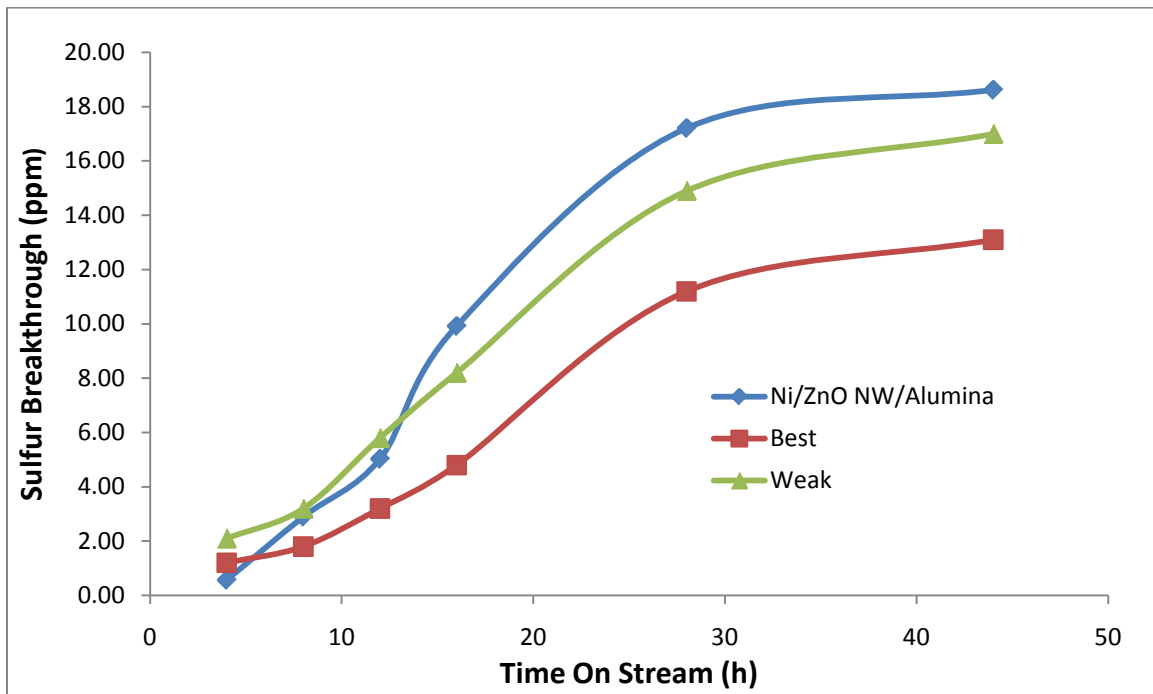


FIGURE 21 – Sulfur Uptake Curves of Two Commercial Catalysts and Ni/ZnO NW/Al₂O₃

V. CONCLUSIONS AND RECOMMENDATIONS

Appreciable quantities of ZnO NWs were prepared and purified for the production of an HDS reactive adsorbent. An active nickel phase was delivered onto the nanowires via simple impregnation and calcination of an aqueous nickel solution. Extensive characterization indicated that nickel – support interaction is stronger when the support is comprised of ZnO NWs rather than ZnO NPs. Stronger interaction favors two key catalyst properties: small nickel crystallite size and lower susceptibility toward sintering. Hydrogenation and HDS activity tests of the prepared catalyst extrusions confirmed activity according to the expected reactive adsorption scheme. However, the performance proved to be inadequate, when compared to existing nickel catalysts. It can reasonably be suspected that the extrusion preparation, calcination, and reduction steps were not at all optimal. The extrusion preparation alone presents ample opportunities for failure. Considering the immaturity of the approach, the prospect for an ultra-deep HDS catalyst still holds true, and as valuable experience was gained, further trials are likely to show improvement.

The routes taken and described in this paper leave a plethora of opportunities for improvement. There are several aspects that emerged during the nanowire production, catalyst preparation, and testing which could easily be improved upon.

For future efforts it is recommended to implement a filter with higher bulk surface area into the NW collection setting of the plasma reactor. Up until now, production runs were limited to about 15 minutes as the current filter system, which has already been improved upon during this work, rapidly clogs up with NWs. There are commercial filter solutions available, which after installment would allow for long steady state production runs.

The most room for improvement lies with the catalyst itself. The criteria for the nickel precursor might not be favorably prioritized or even complete. Literature claims for nano-sized nickel particles are plentiful. It could prove beneficial to extend the nickel precursor search to find a better candidate. Nickel formate, for example, is said to produce particle sizes of 1.2 nm. Therefore, inspecting several more precursors could potentially be rewarding.

The experience gained handling binder materials throughout the research is still limited. As the binder has critical influence over crush strength and surface area it is recommended to explore different materials and extrusion production schemes. Certainly, it would also be interesting to see how the Ni/ZnO NW system performs without any additives at all.

The hydrogenation test runs according to a standardized format. The reduction procedure of 845°F for 16 hours is simply too harsh for the proposed catalyst. Reducing the temperature to 800°F was probably not enough to prevent major sintering and deactivation. The available literature provides conflicting information if reduction is necessary at all. In view of the apparent delicateness of the tested catalyst it is recommended to investigate if in-situ pre-reduction at high temperature is indispensable, or if operating temperatures and regular hydrogen supply is sufficient to activate the catalyst.

Most importantly, it is recommended to characterize the spent catalyst extrusions. Unfortunately, time constraints to conclude this paper, prohibited the execution of several planned tests, that would most certainly have contributed valuable information to this venture.

REFERENCES

- Aguilhon, Julie, et al. 2010. *Nickel nanoparticles with controlled morphologies application in selective hydrogenation catalysis*. Lyon: Rond-point de l' échangeur de Solaize.
- Alonso, F., Riente, P., Sirvent, J., and Yus, M. 2010. Nickel nanoparticles in hydrogen-transfer reductions: Characterisation and nature of the catalyst. *Applied Catalysis A: General* 378:42-51.
- Anandan, K. and Rajendran, V. 2011. Morphological and size effects of NiO nanoparticles via solvothermal process and their optical properties. *Materials Science in Semiconductor Processing* 14: 43-47.
- Andeen, D., et al. 2006. Lateral Epitaxial Overgrowth of ZnO in Water at 90°C. *Advanced Functional Materials* 16:799-804.
- Bezverkhyy, I., et al. 2008. Kinetics of thiophene reactive adsorption on Ni/SiO₂ and Ni/ZnO. *Catalysis Today* 130:199-205.
- Cheng, R., et al. 2010. Dechlorination of pentachlorophenol using nanoscale Fe/Ni particles: Role of nano-Ni and its size effect. *Journal of Hazardous Materials* 180:79-85.
- Clark, Ezra. 2011. Commercializing the Mass Production of Nanowires. J. B. Speed School of Engineering, University of Louisville.
- Costa-Serra, J., Guil-Lopez, R., and Chica, A. 2010. Co/ZnO and Ni/ZnO catalysts for hydrogen production by bioethanol steam reforming. Influence of ZnO support morphology on the catalytic properties of Co and Ni active phases. *International Journal of Hydrogen Energy* 35:6709-6716.
- Davar, F., Fereshteh, Z., and Salavati-Niasari, M. 2009. Nanoparticles Ni and NiO: Synthesis, characterization and magnetic properties. *Journal of Alloys and Compounds* 476:797-801.
- De Jesus, J., Gonzalez, I., Quevedo, A., and Puerta, T. 2005. Thermal decomposition of nickel acetate tetrahydrate: an integrated study by TGA, QMS and XPS techniques. *A Journal of Molecular Catalysis: Chemical* 228:283-291.
- Degen, A. and Kosec, M. 2000. Effect of pH and impurities on the surface charge of zinc oxide in aqueous solution. *Journal of the European Ceramic Society* 20:667-673.

- Deraz, N., Selim, M., and Ramadan, M. 2009. Processing and properties of nanocrystalline Ni and NiO catalysts. *Materials Chemistry and Physics* 113:269-275.
- Desai, A. and Haque, M. 2007. Mechanical properties of ZnO nanowires. *Sensors and Actuators* 134:169-176.
- Dharmaraj, N., et al. 2006. Synthesis of nickel oxide nanoparticles using nickel acetate and poly(vinyl acetate) precursor. *Materials Science and Engineering B* 128:111-114.
- Ding, Y. and Zhong, W. 2009. *Micron* 40:335-342.
- Du, Y., Chen, H., Chen, R., and Xu, N. 2004. Synthesis of *p*-aminophenol from *p*-nitrophenol over nano-sized nickel catalysts. *Applied Catalysis A: General* 277:259-264.
- Erri, P. and Varma, A. 2009. Diffusional Effects in Nickel Oxide Reduction Kinetics. *Ind. Eng. Chem. Res.* 48:4-6.
- Fan, J., et al. 2010. Research on Reactive Adsorption Desulfurization over Ni/ZnO—SiO₂—Al₂O₃ Adsorbent in a Fixed-Fluidized bed reactor. *Ind. Eng. Chem. Res.* 49:8450-8460.
- Farhadi, S. and Roostaei-Zaniyani, Z. 2011. *Polyhedron*.
- Farhadi, S., Kazem, M., and Siadatnasab, F. 2011. NiO nanoparticles prepared via thermal decomposition of the bis(dimethylglyoximate)nickel(II) complex: A novel reusable heterogeneous catalyst for fast and efficient microwave-assisted reduction of nitroarenes with ethanol. *Polyhedron* 30:606-613.
- Feng, L., et al. 2010. Fabrication and characterization of tetrapod-like ZnO nanostructures prepared by catalyst-free thermal evaporation. *Materials Characterization* 61:128-133.
- Han, Y., Li, J., Ning, X., Yang, X., and Chi, B. 2004. Study on NiO excess in preparing NiAl₂O₄. *Materials Science and Engineering A* 369:241-244.
- Hou, Y., Kondoh, H., Ohta, T., and Gao, S. 2005. Size-controlled synthesis of nickel nanoparticles. *Applied Surface Science* 241:218-222.

- Huang, L., et al. 2010. A sulfur K-edge XANES study on the transfer of sulfur species in the reactive adsorption desulfurization of diesel oil over Ni/ZnO. *Catalysis Communications* 11:592-596.
- Huang, L., et al. 2011. In situ XAS study on the mechanism of reactive adsorption desulfurization of oil product over Ni/ZnO. *Applied Catalysis B: Environmental* 106:26-38.
- Ito, E. and Rob van Veen, J. 2006. On novel processes for removing sulphur from refinery streams. *Catalysis Today* 116:446-460.
- Jankovic, B., Adnadevic, B., and Mentus, S. 2007. The kinetic analysis of non-isothermal nickel oxide reduction in hydrogen atmosphere using the invariant kinetic parameters method. *Thermochimica Acta* 456:48-55.
- Kim, J., et al. 2008. Design of an efficient microwave plasma reactor for bulk production of inorganic nanowires. *Informacije MIDEM* 38:237-243.
- Knacke, O. 1991. Thermochemical Properties of Inorganic Substances 2nd Edition. Berlin: Springer-Verlag
- Kobayashi, Y., et al. 2011. Effect of NiO content in mesoporous NiO-Al₂O₃ catalysts for high pressure partial oxidation of methane to syngas. *Applied Catalysis A: General* 395:129-137.
- Kumar, V., et al. 2008. Gas-Phase, Bulk Production of Metal Oxide Nanowires and Nanoparticles Using a Microwave Plasma Jet Reactor. *J. Phys. Chem. C* 112:17750-17754.
- Lee, Y., et al. 2008. The preparation and desulfurization of nano-size ZnO by a matrix-assisted method for the removal of low concentration of sulfur compounds. *Current Applied Physics* 8:746-751.
- Li, Q., Wang, L., Hu, B., Yang, C., Zhou, L., and Zhang, L. 2007. Preparation and characterization of NiO nanoparticles through calcinations of malate gel. *Materials Letters* 61:1615-1618.
- Lif, J., Odenbrand, I., and Skoglundh, M. 2007. Sintering of alumina-supported nickel particles under amination conditions: Support effects. *Applied Catalysis A: General* 317:62-69.
- Liu, H. and Liu, J. 2010. Faceted ZnO nanowire supported Pd catalyst for the Methanol Steam Reforming. *Microsc. Microanal.* 16:1206.

- Liu, Hongyang, Allard, Lawrence, and Liu, Jingyue. 2011. *ZnO nanowire-supported Pd catalyst for methanol steam reforming*. Saint Louis: Center for Nanoscience.
- Mahata, N., Cunha, A., Orfao, J., and Figueredo, J. 2009. Hydrogenation of chloronitrobenzene over filamentous carbon stabilized nickel nanoparticles. *Catalysis Communications* 10:1203-1206.
- Mesters, C. M. A. M. 2007. U.S. Patent 7,297,655.
- Patil, A., Patil, K., and Pardeshi, S. 2010. Ecofriendly synthesis and solar photocatalytic activity of S-doped ZnO. *Journal of Hazardous Materials* 183:315-323.
- Pina, G., Louis, C., and Keane, M. Nickel particle size effects in catalytic hydrogenation and hydrodechlorination: phenolic transformations over nickel/silica. *Phys. Chem. Chem. Phys.* 5:1924-1931.
- Rasmussen, F., et al. 2004. Sintering of Ni/Al₂O₃ catalysts studied by anomalous small angle X-ray scattering. *Applied Catalysis A: General* 267:165-173.
- Ryzhikov, A., Bezverkhyy, I., and Bellat, J. 2008. Reactive Adsorption of thiophene on Ni/ZnO: Role of hydrogen pretreatment and nature of the rate determining step. *Applied Catalysis B: Environmental* 84:766-772.
- Salavati-Niasari, M., Davar, F., and Fereshteh, Z. 2010. Synthesis of nickel and nickel oxide nanoparticles via heat-treatment of simple octanoate precursor. *Journal of Alloys and Compounds* 494:410-414.
- Song, C. 2003. An overview of new approaches to deep desulfurization for ultra-clean gasoline, diesel fuel and jet fuel. *Catalysis Today* 86:211-263.
- Stanislaus, A., Marafi, A., and Rana, M. 2010. Recent advances in the science and technology of ultra low sulfur diesel (ULSD) production. *Catalysis Today* 153:1-68.
- Tang, H., et al. 2011. Enhancement of desulfurization performance of nickel-based adsorbents by hydrogen reduction pretreatment. *Catalysis Communications* 12:1079-1083.
- Tawara, K., et al. 2001. New Hydrodesulfurization Catalyst for Petroleum-Fed Fuel Cell Vehicles and Cogenerations. *Ind Eng. Chem. Res.* 40:2367-2370.

- Tawara, K., Imai, J., and Iwanami, H. 2000. Ultra-deep hydrodesulfurization of kerosene for fuel cell system (part 3): development and evaluation of Ni/ZnO catalyst. *Sekiyu Gakkaishi* 43:105-113.
- Wang, A., Yin, H., Lu, H., Xue, J., Ren, M., and Jiang, T. 2009. Catalytic activity of nickel nanoparticles in hydrogenation of *p*-nitrophenol to *p*-aminophenol. *Catalysis Communications* 10:2060-2064.
- Wang, Y., et al. 2005. Preparation of NiO nanoparticles and their catalytic activity in the thermal decomposition of ammonium perchlorate. *Thermochimica Acta* 437:106-109.
- Wu, Y., He, Y., Wu, T., Weng, W., and Wan, H. 2007. Effect of synthesis method on the physical and catalytic property of nanosized NiO. *Materials Letters* 61:2679-2682.
- Wu, Z., Ge, S., Zhang, M., Li, W., and Tao, K. 2009. Synthesis of nickel nanoparticles supported on metal oxides using electroless plating: Controlling the dispersion and size of nickel nanoparticles. *Journal of Colloid and Interface Science* 330: 359-366.
- Xiang, L., Deng, X., and Jin, Y. 2002. Experimental study on synthesis of NiO nanoparticles. *Scripta Materialia* 47:219-224.
- Zhang, J., et al. 2010. Reactive adsorption of thiophene on Ni/ZnO adsorbent: Effect of ZnO textural structure on the desulfurization activity. *Journal of Natural Gas Chemistry* 19:327-332.
- Zhang, R., Wang, B., Zhang, H., and Wei, L. 2005. Influence of sulfidation ambience on the properties of nanocrystalline ZnS films prepared by sulfurizing the as-sputtered ZnO films. *Applied Surface Science* 245:340-345.
- Zhou, D. and Keller, A. 2010. Role of morphology in the aggregation kinetics of ZnO nanoparticles. *Water Research* 44:2948-2956.

APPENDIX

Supplementary Tables and Figures

TABLE I

ORGANO-SULFUR COMPOUNDS WITH HDS REACTION CONSTANTS


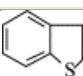
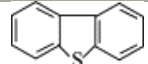
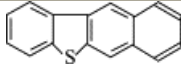
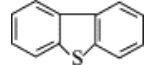
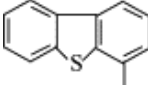
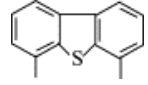
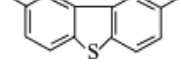
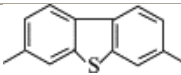
Reactant	Structure	Pseudo-first-order rate k (L/g cat)	Rate constant (min^{-1})
Thiophene		$1.38 \times 10^{-3*}$	
Benzothiophene		$8.11 \times 10^{-4*}$	>0.20 (CoMo) >0.20 (NiMo)
Dibenzothiophene		$6.11 \times 10^{-5*}$	
Benzo[<i>b</i>]naphtho-[2,3- <i>d</i>] thiophene		$1.61 \times 10^{-4*}$	
Dibenzothiophene		$7.38 \times 10^{-5**}$	0.058 (CoMo) 0.057 (NiMo)
4-Methyldibenzothiophene		$6.64 \times 10^{-6**}$	0.018 (CoMo) 0.020 (NiMo)
4,6-Dimethyldibenzothiophene		$4.92 \times 10^{-6**}$	0.006 (CoMo) 0.008 (NiMo)
2,8-Dimethyldibenzothiophene		$6.72 \times 10^{-5**}$	
3,7-Dimethyldibenzothiophene		$3.53 \times 10^{-5**}$	

TABLE II

OVERVIEW OF CATALYST PARTICLE DIMENSIONS, SELECTED REPORTS

ZnO initial (nm)	ZnO final (nm)	NiO (nm)	Ni (nm)	SA (m ² /g)	Group
10	22	11	15		Huang
14		5		32	Bezverkhyy
>200			22	5	Da Costa-Serra
12	15	5	7	34	Ryzhikov
19	28	6	10	29.7	Zhang
20	30			40.7	Lee
				16	Tawara
20				7.4 - 37.8	Zhou
pure nickel or nickel oxide particle diameter, various synthesis methods					
		7.7 - 24.1		123.0 - 16	Wu, Ying
			<10	33	Alonso
			15.1 - 40.1	39	Lif
		5.9 - 7.1	11.7 - 15.9		Kobayashi
		40 - 50			Dharmaraj
		14	22		Fatemeh
		10, 15			Xiang
			30		Cheng
			9		Wang
			57		Du
		19, 30			Mahata
			10		Wang
		24			Salavati-Niasari
		12, 15			Farhadi
			7.8		Pina
		25, 30			Anandan
		40			Wu, Zhijie
		6, 7			Rasmussen
			3, 5, 11		Hou
		12, 14			Li

TABLE III

NANOWIRE SURFACE AREA AND NICKEL LOADING

ρ of ZnO	5606000	g/m ³	(5.606 g/cm ³)	dia NiO NP	7.00E-09
ρ of NiO	6670000	g/m ³	(6.67 g/cm ³)	V NiO drop	8.98E-26
Length NW	0.000001	m	(1000 nm)	Coverage	0.5
Dia NW (nm)	V NW (m ³)	Mass of NW (g)	SA (m ² /g)	Coverage	Mass Ratio
70.0	3.848E-21	2.15744E-14	10.19316039	1.100E-13	0.079
60.0	2.827E-21	1.58506E-14	11.89202045	9.425E-14	0.093
55.0	2.376E-21	1.33189E-14	12.97311322	8.639E-14	0.101
52.5	2.165E-21	1.21356E-14	13.59088052	8.247E-14	0.106
50.0	1.963E-21	1.10074E-14	14.27042455	7.854E-14	0.111
47.5	1.772E-21	9.93414E-15	15.02149952	7.461E-14	0.117
45.0	1.590E-21	8.91596E-15	15.85602727	7.069E-14	0.123
42.5	1.419E-21	7.95281E-15	16.78873476	6.676E-14	0.131
40.0	1.257E-21	7.04471E-15	17.83803068	6.283E-14	0.139
37.5	1.104E-21	6.19164E-15	19.02723273	5.890E-14	0.148
35.0	9.621E-22	5.3936E-15	20.38632078	5.498E-14	0.159
32.5	8.296E-22	4.65061E-15	21.9544993	5.105E-14	0.171
30.0	7.069E-22	3.96265E-15	23.78404091	4.712E-14	0.185
27.5	5.940E-22	3.32972E-15	25.94622645	4.320E-14	0.202
25.0	4.909E-22	2.75184E-15	28.54084909	3.927E-14	0.222
22.5	3.976E-22	2.22899E-15	31.71205454	3.534E-14	0.247
20.0	3.142E-22	1.76118E-15	35.67606136	3.142E-14	0.278
17.5	2.405E-22	1.3484E-15	40.77264156	2.749E-14	0.317
15.0	1.767E-22	9.90662E-16	47.56808182	2.356E-14	0.370
12.5	1.227E-22	6.8796E-16	57.08169818	1.963E-14	0.444
10.0	7.854E-23	4.40294E-16	71.35212273	1.571E-14	0.555
7.5	4.418E-23	2.47665E-16	95.13616363	1.178E-14	0.740
7.0	3.848E-23	2.15744E-16	101.9316039	1.100E-14	0.793

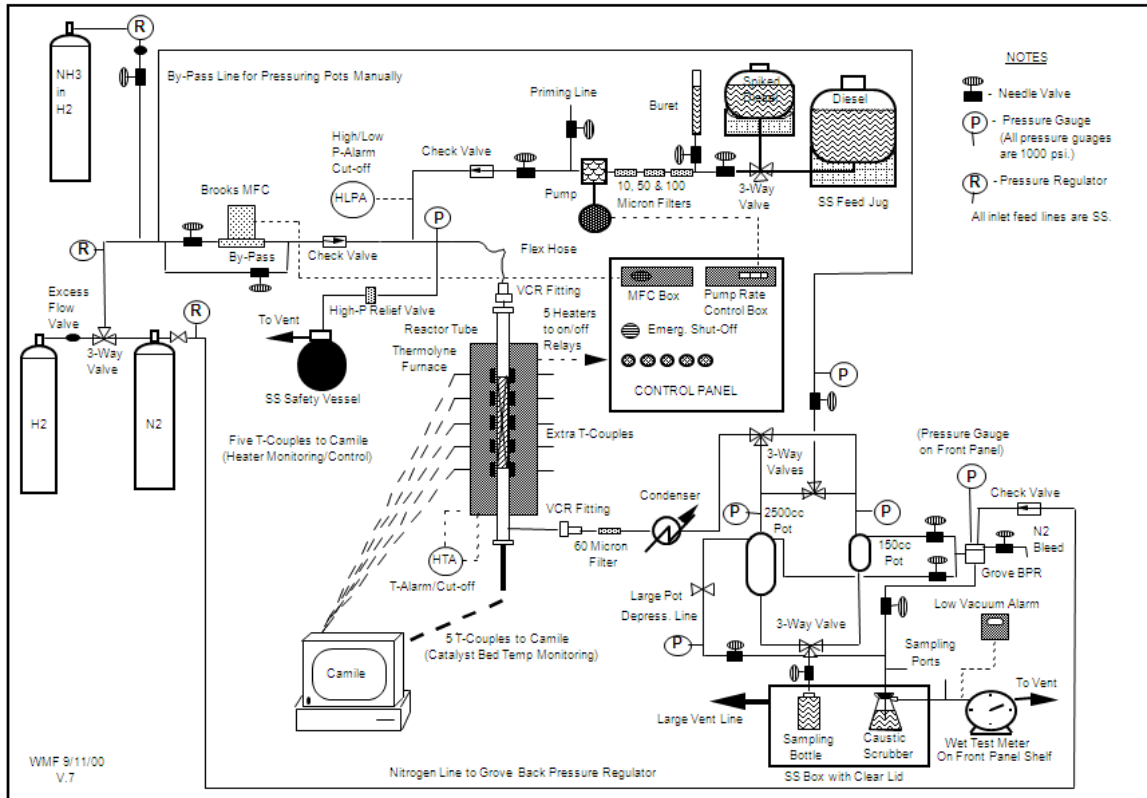


FIGURE 24 –Unit Diagram for Hydrogenation Test Reactor

Raw Data

TABLE V

PRODUCT SAMPLE DILUTION AND UV/VIS RECORD

Test #11-05-03 Ni/ZnO NW Extrusions									
	First Dilution		Second Dilution		Background Points		Peak Point	Net Peak	In Product
HOS	Sample Weight	Total Weight	Sample Weight	Total Weight	246	310	270	270	Percent Aromatics
Feed	0.3968	19.5009	0.4801	20.6929	0.4630	0.0550	0.5260	0.2160	24.800
4	0.1122	2.1045	0.1067	8.2086	0.0040	0.0020	0.0050	0.0018	0.137
8	0.1205	2.1508	0.1059	8.1812	0.0740	0.0090	0.1220	0.0724	5.409
12	0.1141	2.1410	0.1071	8.1315	0.3310	0.0360	0.4540	0.2336	18.041
16	0.1154	2.1192	0.1044	8.1312	0.3390	0.0340	0.4730	0.2484	19.255
20	0.1291	2.1427	0.1069	8.1456	0.4900	0.0580	0.6250	0.2970	20.359
24	0.1246	2.1544	0.1024	8.1513	0.5260	0.0650	0.6430	0.2899	21.626
28	0.1308	2.1743	0.1064	8.1770	0.6210	0.0760	0.7360	0.3194	22.115
32	0.1261	2.1454	0.1060	8.1187	0.6530	0.0800	0.7590	0.3209	22.664
36	0.1246	2.1590	0.1064	8.1209	0.6640	0.0820	0.7630	0.3173	22.742
40	0.1306	2.1548	0.1071	8.1531	0.7130	0.0880	0.8100	0.3314	22.560
44	0.1261	2.1397	0.1077	8.0842	0.7100	0.0880	0.8000	0.3233	22.316
48	0.1254	2.1674	0.1071	7.8257	0.7370	0.0920	0.8240	0.3289	22.513

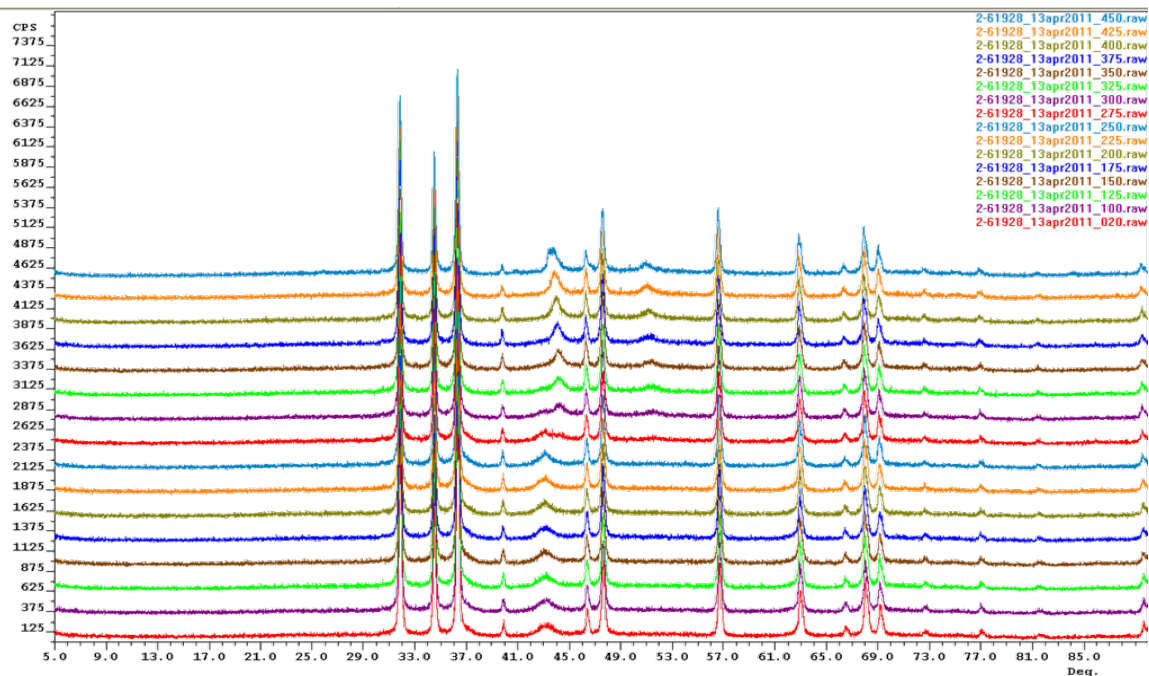


FIGURE 22 – NiO/ZnO NW Reduction Signal under 5% Hydrogen Hot Stage XRD

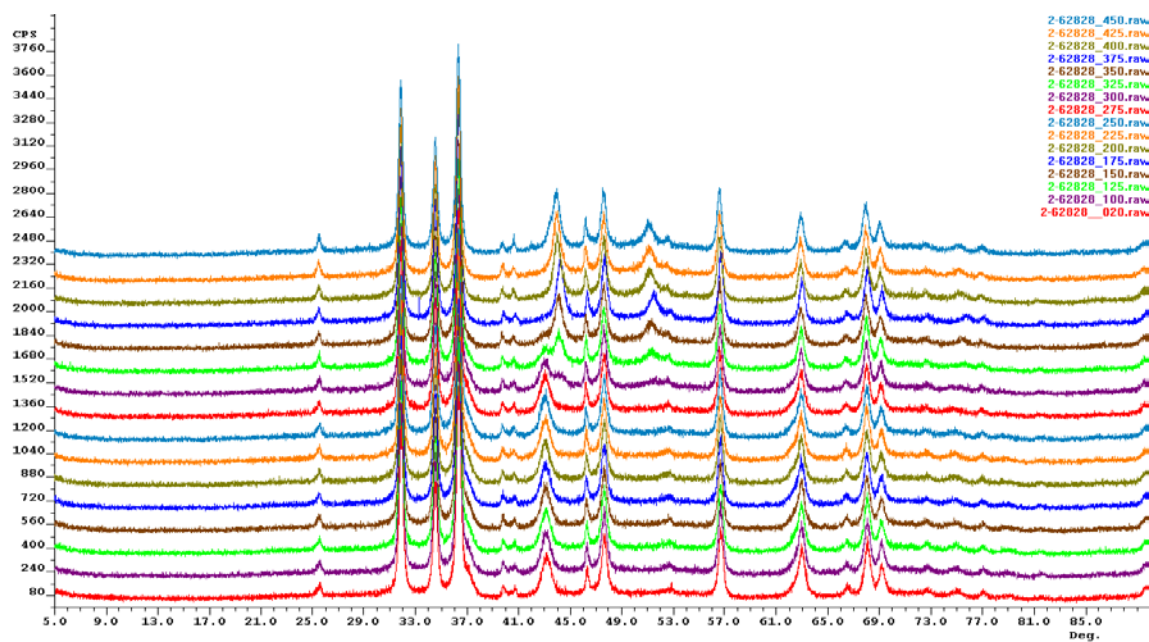


FIGURE 23 – NiO/ZnO NP Reduction Signal under 5% Hydrogen Hot Stage XRD

Photographs

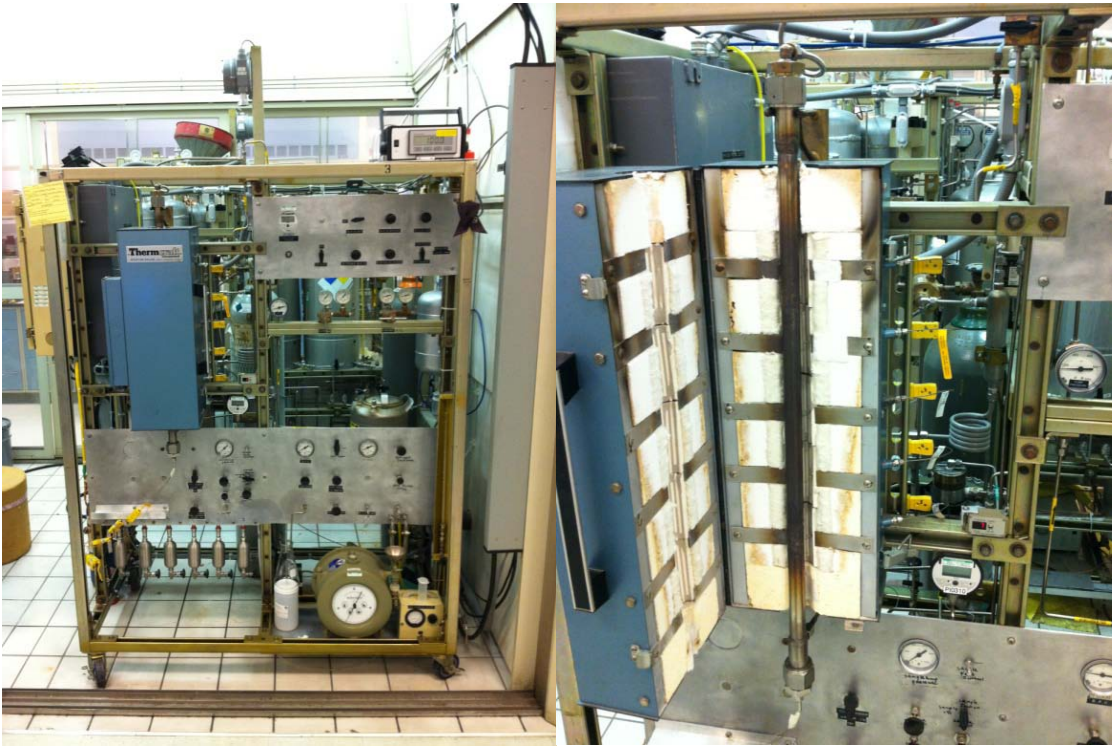


FIGURE 25 – Photographs of Hydrogenation Test Unit



FIGURE 26 – Photographs of the Extrusion Production Process

VITA

The author Franz Petzold was born on 21st of May 1979 in Berlin, Germany where he grew up to adulthood. He received his first bachelor degree of science in business management with a concentration in finance/economics on a track scholarship from ORU. After working in industry for two years in Europe he moved to Louisville, Kentucky where he married his wife Lou Ann Isaacs who he met while at ORU. He combined his new life situation with the move to switch careers to the natural sciences field, for which he developed affection already in childhood. He received his bachelor of science in chemical engineering from the University of Louisville in May of 2010. Feeling comfortable in the academic environment he continued to proceed with his masters in the same field. Dr. Helge Toufar of SCI introduced him to the prospect of collaborating with SCI on a topic relating to hydrogenation/hydrodesulfurization for his master thesis. With Dr. Mahendra Sunkara as his thesis advisor he researched aspects relating a newly proposed catalyst support comprised of zinc oxide nanowires. The above paper resembles the residue of abovementioned collaboration.